



ADVANCED REMOTE SENSING JOURNAL

Volume 2 Issue 1 JUNE 2022



ADVANCED REMOTE SENSING

(VOLUME: 2, ISSUE: 1)

JUNE, 2022

Aim

[Advanced Remote Sensing Journal \(ARSEJ\)](#) publishes regular research papers, reviews, letters, and communications covering all aspects of remote sensing science, from sensor design, validation/calibration, to its application in geosciences, environmental sciences, ecology, and civil engineering. Our aim is to publish novel / improved methods/approaches and/or algorithms of remote sensing to benefit the community, open to everyone in need of them. There is no restriction on the length of the papers or colors used. The method/approach must be presented in detail so that the results can be reproduced. There are, in addition, three unique features of this Journal:

- Manuscripts regarding research proposals and research ideas are welcome
- Electronic files and software regarding the full details of the calculation and experimental procedure, if unable to be published in a normal way, can be deposited as supplementary material
- We also accept manuscripts communicating to a broader audience with regard to research projects financed with public funds

[\(ARSEJ\)](#) is a **Blind Review** and a **free journal**. All of the responsibilities belong to authors.

Scope

Basic remote sensing applications

Multi-spectral and Hyperspectral remote sensing

Active and passive microwave remote sensing (RADAR/SAR)

Lidar and laser scanning

Geometric reconstruction

Image classification and analysis methods

Image processing and pattern recognition

Data fusion and data assimilation

Improvement of atmospheric modelling for radiometric correction

Modelling of parameters obtained from satellite data

Global modelling, monitoring and global database for sustainable development

Checking validity of data by using laboratory and in-situ test methods

Integration of remote sensing and GIS methods

Information utility for reducing disaster and risk effects: Early warning system, Impact assessment, monitoring, flexibility and risk reduction studies

Environmental pollution: Assessment and impact studies

Integration of remote sensing inputs and Earth surface applications

Monitoring growth of agricultural products for sustainable agriculture

Physical modeling and signatures

Change detection

Climate change studies

Global and regional dynamic of land use/biodiversity

Desertification and aridity studies

Soil, vegetation and carbon arc in shore and ocean water

Water quality studies

Dedicated satellite missions

Operational processing facilities

Spaceborne, airborne, unmanned aerial vehicle (UAV) and terrestrial platforms

EDITORIAL BOARD

Editor

Prof. Dr. Murat Yakar, Mersin University, Department of Geomatics Engineering (myakar@mersin.edu.tr)

Co-Editor

Prof. Lachezar Hristov Filchev, Bulgarian Academy of Sciences, Bulgaria (lachezarhf@gmail.com)

Editorial Board

Prof. Mohamed Fouad Abdel Aziz Soliman, Arish University, Faculty of Arts, Egypt (mi_me46@yahoo.com)
(mohamed.fouad2005@yahoo.com)

Dr. Mohamed Atallah (atallahm763@gmail.com)

Prof. *Muhammed Bilal*, School of Marine Sciences, Nanjing University of Information Science & Technology, China (muhammad.bilal@connect.polyu.hk)

Assoc. Prof. Dr. Abel Ramoelo, University of Pretoria, South Africa (abel.ramoelo@gmail.com)

Prof. Dr. Khalil VALIZADEH KAMRAN, University of Tabriz, Faculty of Planning and Environmental Sciences, Iran (valizadeh@tabrizu.ac.ir)

Assoc. Prof. Dr. Eng. Ahmed Serwa, Mataria Helwan University, ahmed_serwa@yahoo.com

Asst. Prof. Atta-ur-Rahman, University of Peshawar, Pakistan (atta-ur-rehman@uop.edu.pk)

Asst. Prof. Ghani Rahman, University of Gujrat, Pakistan (ghanigeo@gmail.com)

Abdell Aziiz Fatthii Abdell Aziiz Ellfadally, Basilicata University / Italian National Research Councils/ National Authority for Remote Sensing and Space Sciences, Italy (abdelaziz.elfadaly@narss.sci.eg) / (abdelaziz.elfadaly@imaa.cnr.it)

Asst. Prof. Dr. KAMAL SROGY DARWISH, Minia University, Egypt (kamal.srogy@mu.edu.eg / kamalelsrogy@gmail.com)

Dr. Milad Janalipour Toosi University of Tech., Tehran – Iran (milad_janalipour@ari.ac.ir)

Asst. Prof. Dr. Mustafa ÜSTÜNER (Artvin Çoruh University) mustuner@artvin.edu.tr

Mohamed Ahmed Badawi Attallah (atallahm763@gmail.com) (atallahm763@gmail.com)

Bello Abubakar Abubakar, Geography Teacher, Islamic Learning Centre (abubakarbello1064@gmail.com)

Dr. Mamadou TRAORE, Central African Republic (matraba77@gmail.com)

Dr. Hashir Tanveer, University of Alabama (hashirrana3@gmail.com)

Dr. AQIL TARIQ (Wuhan University, Wuhan 430079, China) State Key Laboratory of Information Engineering in Surveying Mapping and Remote Sensing (LIESMARS) (aqiltariq@whu.edu.cn /aqiltariq85@gmail.com)

Dr. Sawaid ABBAS (The Hong Kong Polytechnic University, Hong Kong) (sawaid.abbas@gmail.com; sawaid.abbas@connect.polyu.hk)


Dr. Thapa Pawan (Kathmandu University, Dhulikhel, Nepal) pawan.thapa@ku.edu.np

Contents

Lake Meke drought analysis between 2017-2021 with planet multispectral data	1-7
Hasan Bilgehan Makineci	
Investigation of spatial change in Lake Surface with Google Earth Engine: Example of Marmara Lake	8-15
Ramazan Gungor, Osman Salih Yilmaz, Fusun Balik Sanli, Ali Murat Ates	
Determination of city change in satellite images with deep learning structures	16-22
Mustafa Emre Dos	
Integration of Sentinel-1 and Landsat-8 images for crop detection: The case study of Manisa, Turkey	23-33
Muslum Altun, Mustafa Turker	
Analyzing rice farming between sowing and harvest time with Sentinel-1 SAR data	34-39
Ahmet Batuhan Polat, Fusun Balik Sanli, Ozgun Akcay	



Lake Meke drought analysis between 2017-2021 with planet multispectral data

Hasan Bilgehan Makineci*¹ 

¹Konya Technical University, Department of Geomatics Engineering, Türkiye, hbmakineci@ktun.edu.tr

Cite this study: Makineci, H. B. (2022). Lake Meke drought analysis between 2017-2021 with planet multispectral data. *Advanced Remote Sensing*, 2(1), 1-7

Keywords

Lake Meke
NDWI
Planetscope
Temporal Analysis
Wetland Analysis

Research Article

Received: 20.05.2022
Revised: 16.06.2022
Accepted: 21.06.2022
Published: 30.06.2022

Abstract

The city of Konya is experiencing intense drought stress and feels the threat of desertification most intensely. Due to the uncontrolled use of water resources and irregular precipitation regime, Karapınar and its surroundings faced the danger of desertification in a short time. Lake Meke, which has been facing drought for many years, has been the subject of remote sensing research in recent years, with the widespread use of high-resolution satellite data. In this study, the temporal variation of Lake Meke between 2017 and 2021 for March was determined using 3 m spatial resolution multispectral Planetscope data. Wetland changes were determined using the Normalized Difference Water Index (NDWI) for each year of wetland boundaries. As a result, it was determined that the wetlands, which were relatively more in 2017 and 2018, experienced almost complete drought in 2021. When the surface area of wetlands is calculated, it was determined that there was approximately 75% wetland loss between the most significant area and the smallest area between 2017 and 2021.

1. Introduction

Drought is driving itself sensed on our planet and shows its effect by increasing day by day [1, 2]. Most of the research on drought covers large-scale wetlands such as lakes and streams [3]. The temporal analysis of wetlands of this size with remote sensing data has been achieved more frequently in the last quarter-century [4].

Our country, which connects the continents of Europe and Asia, has become a transition country in terms of drought. Due to desertification and rapid consumption of water resources, different problems occur regarding usable water resources in other geographical regions [5]. Konya, located in the Central Anatolia Region and is the largest city in Turkey in terms of surface area, is also in the most dangerous position in periods of drought and desertification [6]. Especially in and around Karapınar District, water use has been a big problem for years [7]. Known as the "Evil Eye Bead of the World", Lake Meke is more than affected by the danger of drought [8, 9].

There are different studies on determining drought as the metric. PDSI (Palmer Drought Severity Index) values are estimated using machine learning methods to predict drought values after one, three and six months [10]. Primary indices such as The Standardized Rainfall Index (SPI) and the Normal Percentage Index (PNI) are also used in drought analyses on a monthly, annual and seasonal scale [11]. Konya Closed Basin (KCB) is one of the regions where the effects of drought are felt the most due to its semi-arid climate. In the research, which analyzed the KCB region between 1998 and 2015 in terms of severity, duration and impact area of drought, seven long dry periods took place, and the most severe and the highest average impact area was experienced in the period of 2006 December - 2007 October [12].

Meke Lake is a fantastic place visually and has an essential position as a wetland in the Konya Closed Basin. Due to biodiversity, Lake Meke, an essential lake, also has an important place for the Karapınar District. In the

region, where agricultural activities have significantly increased over the years, drought has increased, while water consumption has increased [13].

This research carried out a drought analysis of Lake Meke and its surroundings with temporal remote sensing data. The spatial water body was produced from PlanetScope data using the Normalized Difference Water Index (NDWI). As a result, it has been determined that wetlands are gradually decreasing in 2019, 2020, and 2021 compared to 2017 and 2018.

2. Material and Method

In this study, data with the most appropriate visibility were determined and downloaded from the PlanetScope system with a spatial resolution of 3 m in March, the month when the wetlands were the widest. The obtained data were first processed as RGB images with appropriate band combinations. The suitable filter was searched for sharpening the data and enriching the details, and the RGB data were optimized with the Arithmetic Average Filter. In order to reveal the wetland areas, the data for each year was arranged with the NDWI index. Afterwards, necessary analyzes were made, and Change Detection was carried out. As a result of this, drought analysis was carried out depending on the wetland changes (Figure 1).

This study produced NDWI indices using PlanetScope multispectral (MS) 3m spatial resolution data. In addition, the Arithmetic Mean Filter (3×3 pixels) was applied to NDWI images with five iterations to enrich and sharpen the wetlands in the images.

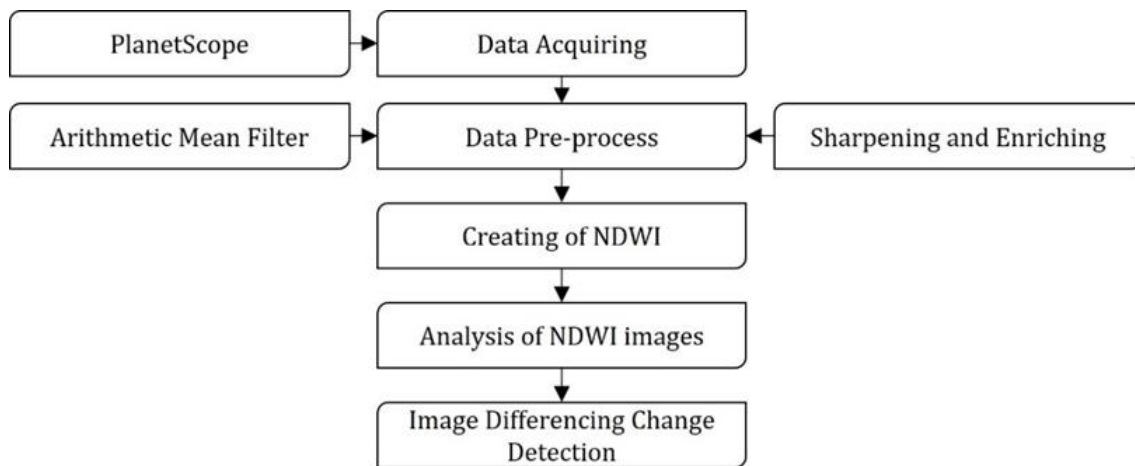


Figure 1. Workflow of the study

2.1. Study Area

Lake Meke, which is located at an altitude of approximately 980 m above sea level and is a volcanic structure, has been known as the "Evil Eye Bead of the World" for years because it looks like a black dot in the middle of its blue waters [9]. The red appearance formed by the shrinking wetlands is due to living microorganisms. It was included in the Ramsar Convention, an international convention aimed at protecting and sustaining wetlands, in 2005 [14, 15]. Lake Meke, which was selected for the study area of this research, is located in Turkiye, as presented in Figure 2.

2.2. PlanetScope Remote Sensing Data

PlanetScope constellation satellites consist of data from multiple launched satellite clusters, each in the form of cube satellites (DOVEs). The Sun-synchronous constellation system has the Ground Sampling Distance (GSD) in the nadir direction is 3.9 meters (Table 1). Multispectral data is presented in 4 bands (RGB+Near Infrared). PlanetScope orthomosaic data is given to users with radiometric calibrated, and sensor corrections are applied, orthorectified, and converted into a UTM projection.

Since the overall area of Lake Meke's wetlands is not particularly large, using satellite data with a high spatial resolution is more helpful in finding actual wetlands. For this reason, analyzes were made using PlanetScope high-resolution MSI images.

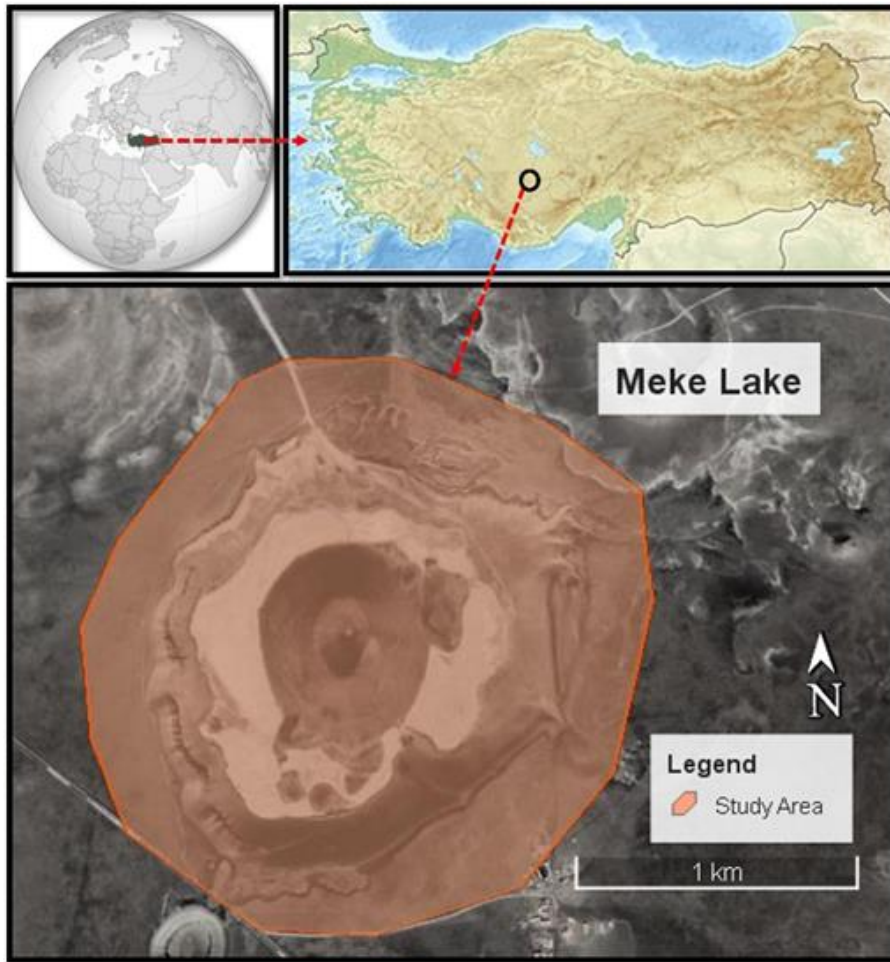


Figure 2. Study area

Table 1. Remote sensing data specs

Data Type	Date of Acquisition	Spatial Resolution	Bands
AnalyticMS-SR	03/22/2017	~3 m	RGB+NIR
AnalyticMS-SR	03/21/2018	~3 m	RGB+NIR
AnalyticMS-SR	03/23/2019	~3 m	RGB+NIR
AnalyticMS-SR	03/22/2020	~3 m	RGB+NIR
AnalyticMS-SR	03/19/2021	~3 m	RGB+NIR

2.3. NDWI

NDWI is used to reveal wetlands' temporal changes occurrences by remote sensing [16-18]. It is based on a different combination and normalization of the bands (Equation 1). If the reflectance values are more significant than 0.5 in the result obtained, these areas generally correspond to water bodies.

$$NDWI = \frac{Band\ 2\ (Green) - Band\ 4\ (NIR)}{Band\ 2\ (Green) + Band\ 4\ (NIR)} \quad (1)$$

2.4. Arithmetic Mean Filter

The filter, known as the arithmetic mean filter, is a preferred image processing for sharpening and enriching the details in images. Sharpening and enriching provide convenience in the study and eliminate some errors caused by image acquisition. The arithmetic mean filter, which has been tried on data and has shown successful

results, has been preferred because of its positive effects on evaluating results. When used as 3×3 , it serves to rearrange the image using the arithmetic means of eight different neighbors of a pixel. The mean filter is a simple way to reduce noise in an image. If the size of the template matrix increases (like 5×5 or 9×9), the smoothing will increase even more.

2.5. Image Differencing Change Detection

The registered, normalized multi-temporal satellite images could be subjected to four of the most widely used change detection techniques. These techniques comprise post-classification, image differencing, image rationing, and principal components analysis (PCA).

The digital number (DN) value of a pixel for a specific band on one date is deducted from the DN value of the same pixel for the same band on another date to conduct the image differencing change detection approach [19, 20]. Three different images for the three bands, red, green, and blue, were produced via pixel-by-pixel subtraction of each band from image 2017 to 2021.

3. Results

As a result of the data evaluation for March of five different years belonging to Lake Meke, the surface area changes of the wetlands over the years (2017-2021) have been visually determined and presented in Figure 3. Change detection performed in this investigation is also presented in Figure 4. Relative accuracy can be mentioned when evaluating the findings. For this reason, no accuracy assessment was carried out in the research. Since the study area is not very large, it is assumed that the errors caused by the satellite data and the rough errors caused by the operator do not have a large percentage.

Table 2. Change detection of Meke Lake between 2017-2021

Data Type	Date of Analysis	Total of Wetland and Humid Lands (Ha)	Amount of Change (Ha)
AnalyticMS-SR	03/22/2017	~38.4	-
AnalyticMS-SR	03/21/2018	~45.5	~+7.1
AnalyticMS-SR	03/23/2019	~18.9	~-25.6
AnalyticMS-SR	03/22/2020	~14.1	~-4.8
AnalyticMS-SR	03/19/2021	~10.2	~-3.9

The evaluation was made on wetland, humid land, and dry land. When evaluated like this, the wetlands of Lake Meke, which had an increasing trend in 2017 and 2018, drought sharply in 2019, and in 2020 and 2021, the drought continued, and Meke Lake was almost wholly drought out (Table 2).

4. Discussion

Previous research has stated that Lake Meke and the Konya Closed Basin, where it is located, experience drought and will completely dry out in the coming years. Dogan, Berkay [8], in his drought analysis study covering the years between 1972 and 2009, revealed the drought threat for the Konya Closed Basin. Information has been provided that Lake Meke, located in the study area, is also under the threat of drought. Celebi [13] has stated that while there were 45,000 wells and 1,760,456 hectares of cultivated land in 2002, there were over 100,000 wells and 2,023,513 hectares of cultivated land in 2011 in the Konya Closed Basin. Some have entirely dried up, such as the Hotamış and Eşmekaya marshes, and also some wetlands like Ereğli marshes, Salt Lake, Beyşehir Lake, Meke Lake and Samsam Lake have decreased by about approximately 30-85%. Even though the research and findings that have been going on for years revealed the threat of drought, and it has been stated that agricultural activities accelerate the drought in the region, it is seen that no precautions are taken, and the region is left to fate. As a result, it is seen that the drought experienced in Lake Meke is a situation from the past. Although this study, which was carried out between 2017 and 2021, is not based on the data obtained from the field, it is essential to reveal the change in the surface area. It is possible to say that Lake Meke has been exposed to an irreversible drought.

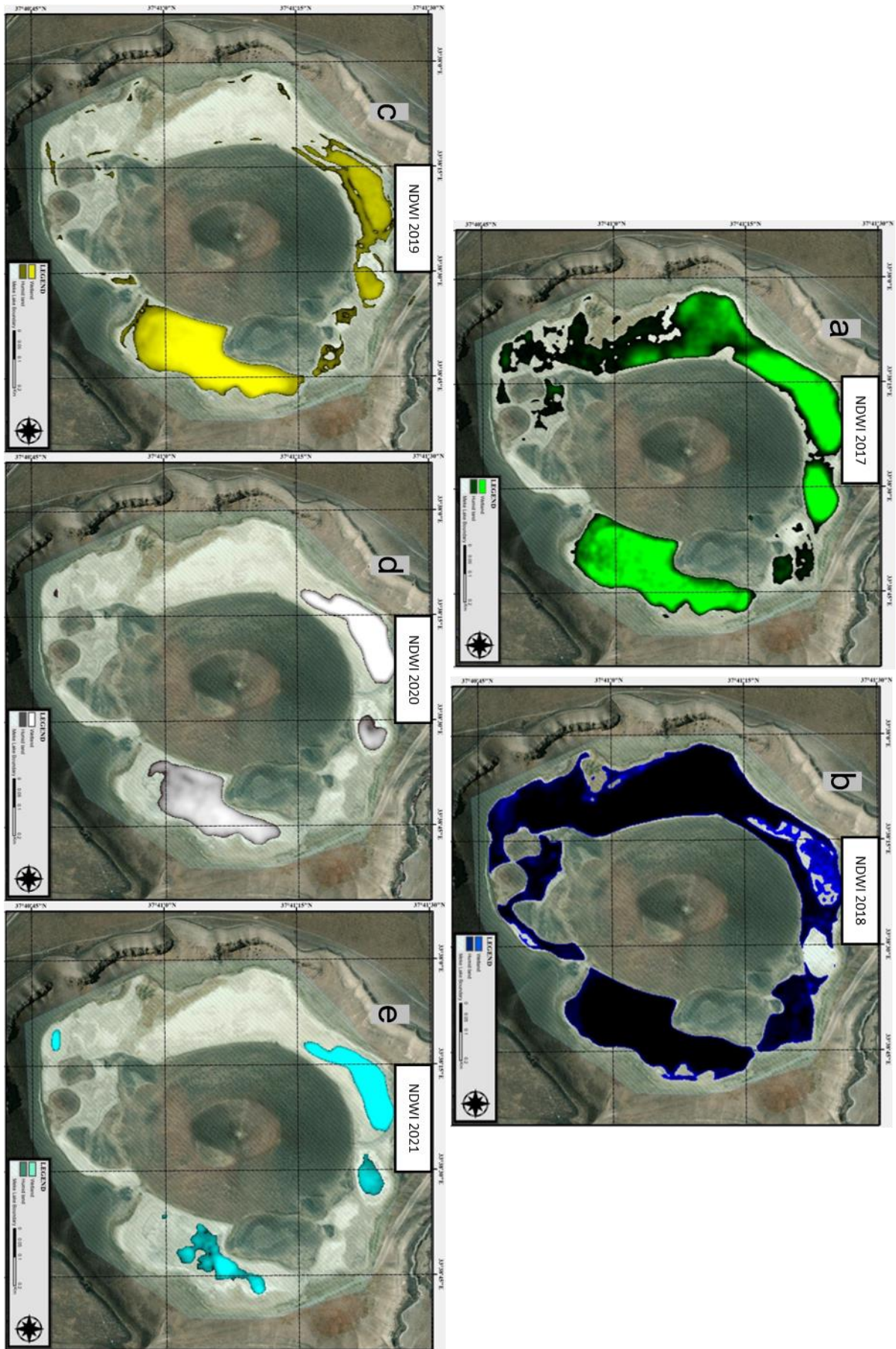


Figure 3. Wetland analysis from March data and change detection (a: the year 2017, b: the year 2018, c: the year 2019, d: the year 2020, e: the year 2021)

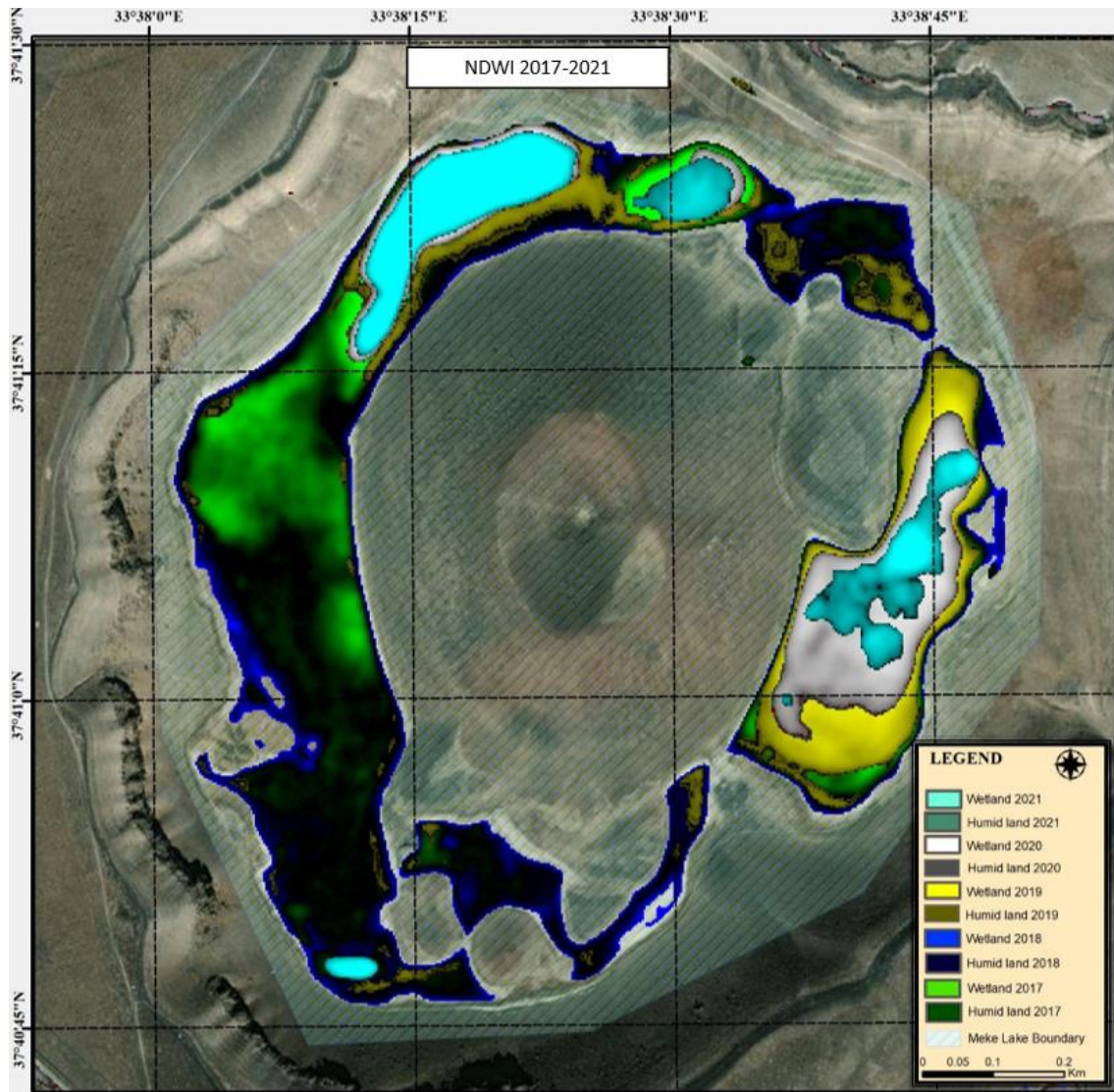


Figure 4. Change detection analysis from 2017-2021

5. Conclusion

This study successfully performed temporal drought analysis of Lake Meke in Karapınar District of Konya Province with PlanetScope 4-band MS remote sensing data. From the March data for the years 2017-2021, new results of the NDWI indices were produced, wetlands and humid lands were determined, and change detection analyzes were obtained. It has been revealed the wetland area of Lake Meke, which was about 38 hectares in 2017, decreased to about 10 hectares in 2021. Using data sources such as PlanetScope constellations in monitoring studies of tiny wetlands, where the spatial resolution of the Landsat and Sentinel satellite data used by the researchers as free of charge satellite data is insufficient, can be said to be the most significant contribution to the literature of this study.

Acknowledgement

I would like to express my endless thanks to Planet management for providing the multispectral satellite images used in this study for free academic debate. This study was presented as an oral presentation at the XI. TUFUAB symposium and was selected for publication in the journal as a full text.

Funding

This research received no external funding.

Conflicts of interest

The authors declare no conflicts of interest.

References

1. Ault, T. R. (2020). On the essentials of drought in a changing climate. *Science*, 368(6488), 256-260.
2. Monjo, R., Royé, D., & Martin-Vide, J. (2020). Meteorological drought lacunarity around the world and its classification. *Earth System Science Data*, 12(1), 741-752.
3. Mullin, M. (2020). The effects of drinking water service fragmentation on drought-related water security. *Science*, 368(6488), 274-277.
4. Aksoy, S., & Sertel, E. (2021, August). Comparison of drought monitoring indices derived from MODIS and CHIRPS data using Google Earth Engine. In *9th Global Conference on Global Warming (GCGW-2021), Croatia*, 4p.
5. Bacanlı, Ü. G., & Akşan, G. N. (2019). Drought analysis in Mediterranean region. *Pamukkale Üniversitesi Mühendislik Bilimleri Dergisi*, 25(6), 665-671.
6. Sariş, F., & Gedik, F. (2021). Konya Kapalı Havzası'nda meteorolojik kuraklık analizi. *Coğrafya Dergisi*, (42), 295-308.
7. Terzi, Ö., & Ersoy, T. (2018). Yapay sınır ağları ile Konya ili kuraklık tahmini. *DSİ Teknik Bülteni*, (127), 1-13.
8. Dogan, S., Berktaş, A., & Singh, V. P. (2012). Comparison of multi-monthly rainfall-based drought severity indices, with application to semi-arid Konya closed basin, Turkey. *Journal of Hydrology*, 470, 255-268.
9. Öztürk, A., & Horasan, B. Y. (2020). Dünya' da karstik jeopark turizmi ve jeopark öneri alanı: Karapınar (Konya-Türkiye). *Konya Mühendislik Bilimleri Dergisi*, 8(4), 876-888.
10. Başakın, E. E., Ekmekcioğlu, Ö., & Özger, M. (2019). Makine öğrenmesi yöntemleri ile kuraklık analizi. *Pamukkale Üniversitesi Mühendislik Bilimleri Dergisi*, 25(8), 985-991.
11. Çelik, M. A., & Gülersoy, A. E. (2018). Climate classification and drought analysis of Mersin. *Manisa Celal Bayar Üniversitesi Sosyal Bilimler Dergisi*, 16(1), 1-26.
12. Yılmaz, M. (2017). Drought analysis of Konya closed basin with the use of tnpa satellite-based precipitation data. *Journal of the Faculty of Engineering and Architecture of Gazi University*, 32(2).
13. Celebi, M. (2016). Ecological Importance of wetlands and samples in Konya Closed Basin. *International Journal of Scientific Research in Science & Technology*, 2(3), 323-333.
14. Arı, Y. (2006). Ramsar Sözleşmesi'nin doğa koruma yaklaşımına eleştirel bir bakış. *Doğu Coğrafya Dergisi*, 11(15), 275-302.
15. Goodwin, E. J. (2017). Convention on Wetlands of International Importance, Especially as Waterfowl Habitat 1971 (Ramsar). *Elgar Encyclopedia of Environmental Law; Edward Elgar Publishing Limited: Cheltenham, UK*, 101-108.
16. Gao, B. C. (1996). NDWI—A normalized difference water index for remote sensing of vegetation liquid water from space. *Remote sensing of environment*, 58(3), 257-266.
17. Makineci, H. B. (2022). Seasonal drought analysis of Akşehir Lake with temporal combined sentinel data between 2017 and 2021 spring and autumn. *Environmental Monitoring and Assessment*, 194(8), 1-17.
18. Çağlayan, E. B., Furkan, E., Samur, E. B., Deniz, M., Mobariz, M. A., & Kaplan, G. (2020). Uzaktan Algılama Teknikler ile Akşehir Gölü'ndeki Alansal Değişiminin İzlenmesi. *Türkiye Uzaktan Algılama Dergisi*, 2(2), 70-76.
19. Afify, H. A. (2011). Evaluation of change detection techniques for monitoring land-cover changes: A case study in new Burg El-Arab area. *Alexandria engineering journal*, 50(2), 187-195.
20. Lu, D., Mausel, P., Brondizio, E., & Moran, E. (2004). Change detection techniques. *International journal of remote sensing*, 25(12), 2365-2401.



© Author(s) 2022. This work is distributed under <https://creativecommons.org/licenses/by-sa/4.0/>



Advanced Remote Sensing

<http://publish.mersin.edu.tr/index.php/arcej>

e-ISSN 2979-9104



Investigation of spatial change in Lake Surface with Google Earth Engine: Example of Marmara Lake

Ramazan Gungor^{*1}, Osman Salih Yılmaz¹, Fusun Balik Sanlı², Ali Murat Ates³

¹Manisa Celal Bayar University, Geographical Information Systems Department, Türkiye, ramazan.gungor@cbu.edu.tr ; osmansalih.yilmaz@cbu.edu.tr

²Yıldız Technical University, Geomatics Engineering Department, Türkiye, fbalik@yildiz.edu.tr

³Manisa Celal Bayar University, Computer and Instructional Technologies Department, Türkiye, murat.ates@cbu.edu.tr

Cite this study: Gungor, R., Yılmaz, O. S., Sanlı, F. B., & Ateş, A. M. (2022). Investigation of spatial change in Lake Surface with Google Earth Engine: Example of Marmara Lake. *Advanced Remote Sensing*, 2(1), 8-15

Keywords

Remote Sensing
Google Earth Engine (GEE)
NDWI
Support vector machine
Drought

Research Article

Received: 21.05.2022

Revised: 17.06.2022

Accepted: 23.06.2022

Published: 30.06.2022

Abstract

It is essential to monitor the changes in wetlands on the earth's surface to understand the impact of global climate changes and human activities on water resources. Remote Sensing (RS) techniques are beneficial in monitoring and mapping the dynamics of changes in wetlands. Although RS techniques seem practical in monitoring water surfaces, traditional RS methods require a high amount of workforce, software, hardware, and especially data storage needs. For this purpose, in this study, the change in water surface area of Marmara Lake, located within the borders of Manisa Province, between 2013-2022, was investigated with Google Earth Engine (GEE). The change in the water surface area was analyzed for four different seasons using Landsat-8 (OLI) images. The Normalized Difference Water Index (NDWI) was used in the study. The study is divided into four different classes according to the land use conditions of the region: vegetation, water surface, bare lands, and agricultural lands. Support Vector Machines (SVM), a machine learning algorithm, were used for classification. According to the analyzes made, it has been determined that a wetland of 3,975.78 ha has dried up in the lake surface area in the last eight years. This calculated area corresponds to an area of 75.04%, according to the average of all areas.

1. Introduction

Water is undoubtedly the most valuable resource for living things and an essential ecosystem component. Climatic changes and human activities are significant for managing water resources for sustainable socio-economic development [1]. At the same time, wetlands are a valuable natural resource for groundwater recharge and flood control [2]. However, the reduction and destabilization of wetlands pose a significant threat to biodiversity conservation and the ecological environment [3]. Therefore, the mapping and recording of wetlands play an essential role in the planning, protecting, and managing of wetlands [4]. In general, wetlands are part of the topography. They are considered one of the crucial ecosystems consisting of water, vegetation, soil, and microorganism systems and play an essential role in protecting the aquatic ecosystem [5].

Extraction of water bodies plays a vital role in wetland management, assessing water cover status, and detecting and monitoring surface water exchange [6]. Furthermore, thanks to satellite data, remote sensing (RS)

techniques assist in monitoring temporal changes in water bodies and establishing decision-making policies [7]. RS is highly preferred, so it is cost-effective, fast, reliable, reproducible, challenging to access for larger areas, and an effective technique [8].

Landsat images are advantageous to other satellite platforms in temporal tracking water surfaces, thanks to an archive of approximately 40 years and free access [9]. Furthermore, monitoring water surfaces is convenient with various machine learning algorithms and specially developed water extraction indexes on satellite images [10]. For example, the Normalized Difference Water Index (NDWI) uses the green and infrared bands to distinguish between water, soil, and terrestrial vegetation [11]. The modified NDWI (MNDWI) was proposed by using Short-Wave-Infrared (SWIR) band instead of the Near-Infrared (NIR) band, which used NDWI due to vegetation cover soil characteristics, and the effect on built-up areas in the detection of water surfaces. Soil, vegetation, and resident classes have lower negative values because they reflect more of the SWIR band than the green band. Various methods have been proposed for the detection of water surfaces. These can be threshold determination over a calculated index [12-14], or different classification algorithms are used. These; Random Forest (RF), Support Vector Machines (SVM), and Maximum Likelihood Classification (MLC) are frequently preferred methods [15-20].

Satellite data analysis reaching thousands of gigabytes is laborious and time-consuming for long time-series data [21]. In addition, the availability of suitable software and storage space appear as additional costs for data processing. Google Earth Engine (GEE), which works in the cloud platform and has been highly preferred in RS studies in recent years, provides access to all archives of Landsat data [22]. The Google firm developed GEE to map human settlements over large areas, study past changes, and continually update current estimates [23]. Thanks to its application program interface (API), GEE provides the opportunity to develop with JavaScript and Python languages and access and apply data at a petabyte-scale [24].

Today, climatic changes cause severe effects on the ecosystem, especially water resources. Climatic changes such as global warming cause severe effects on lakes, which are freshwater sources. Depleting water resources, especially in developing countries such as Türkiye, causes severe pressures on the country's economy and policy [18]. Marmara Lake, located within the borders of Manisa Province in the Aegean region, is among the lakes of great importance, especially regarding agricultural irrigation and fishing activities.

In this study, the temporal analysis of the change of Marmara Lake was examined using Landsat images on the GEE platform. Considering the characteristic land use of the region, the study area, which is divided into four different classes, is classified by the SVM machine learning algorithm. In addition, NDWI has been added to the classification as a new band because it differentiates it from other details by increasing the reflection values on the water surface. This study determined quantitative and qualitative temporal and spatial changes on the water surface between 2013-2022. It has been revealed that monitoring the changes in the water body of Marmara Lake, which is of great importance, especially for the region, is relatively easy with RS techniques. In addition, thanks to the code developed on the GEE platform, the Marmara Lake change will be realized dynamically and instantly in the coming years. In addition to providing a robust data analysis for decision-makers, this study also creates a database for climate change monitoring, agricultural activities, lake water use, and fishing and hunting activities in the region.

2. Material and Method

2.1. Study Area

The Marmara Lake, which was analyzed within the scope of the study, is within the borders of the Salihli and Gölarmara districts of Manisa province, located in the Aegean Region. The lake is an alluvial barrier lake within the depression area due to the breaking of faults in the north, west, and southeast directions within the Gediz graben. Marmara Lake, which is approximately 10-11 km in the east-west direction and approximately 3-5 km in the north-south direction, is spread over approximately 56 km². The lake's depth varies between 3-5 m according to the water surface area, and it is at an average height of 79 m from the sea [25]. Lake water irrigates agricultural lands around the Ahmetli district within the Lower Gediz Irrigation Project [26]. The study area is shown in [Figure 1](#).

2.2. Data

This study used Landsat-8 (OLI) satellite images of the 2013-2022 time series (Collection 1 Tier 1 calibrated Top of Atmosphere, TOA) to monitor the water surface area change in Marmara Lake. The Landsat-8 satellite has a temporal resolution of 16 days from an altitude of about 705 km. The images obtained from the OLI sensor of this satellite have an area of 180 km and a 12-bit radiometric resolution. The sensor records geometrically corrected images in the VIS, NIR, and SWIR spectral regions for nine spectral bands with a spatial resolution of 30 m and panchromatic bands with a resolution of 15 m. Satellite images were analyzed seasonally, and images with less than 15% cloud coverage were generally selected. The band information of the satellite image used in this study is given in [Table 1](#).

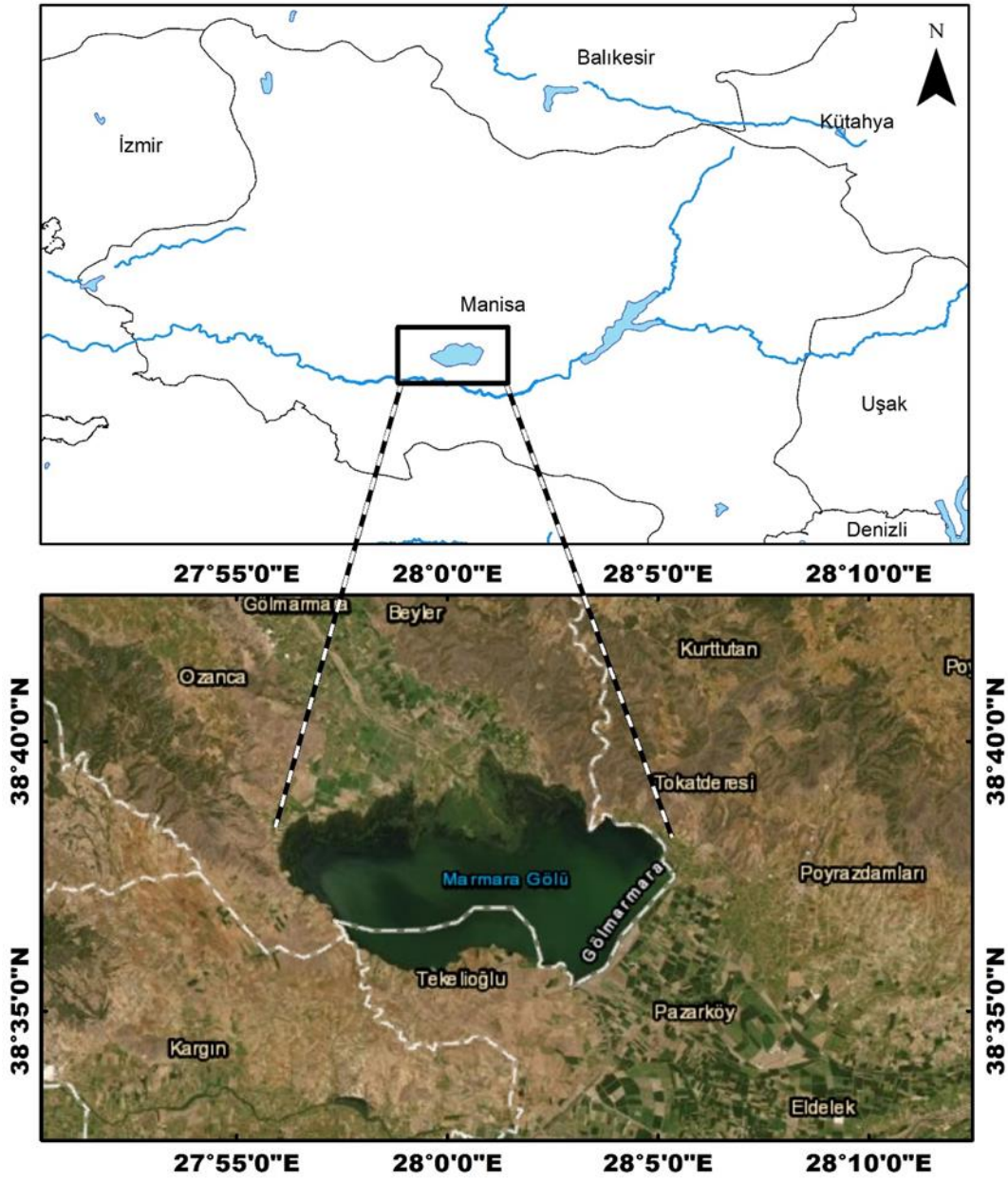


Figure 1. Study area

Table 1 The spectral bands and resolutions of optical Landsat 8 datasets used in this study

Spectral Range	Wavelength Range (μm)	Resolution (m)
Blue (B2)	0.45-0.51	30
Green (B3)	0.53-0.59	30
Red (B4)	0.64-0.67	30
NIR (B5)	0.85-0.88	30
SWIR 1 (B6)	1.57-1.65	30

2.3. Method

First, NDWI was calculated using Landsat -8 (OLI) satellite images to monitor the temporal changes on Marmara Lake's water surface. In the second step, the classification process was done with the SVM algorithm. In the third step, an accuracy assessment was performed for each classified image. Then, all classification maps were converted to raster vectors, and lake surface areas were calculated. The flowchart is given in Figure 2.

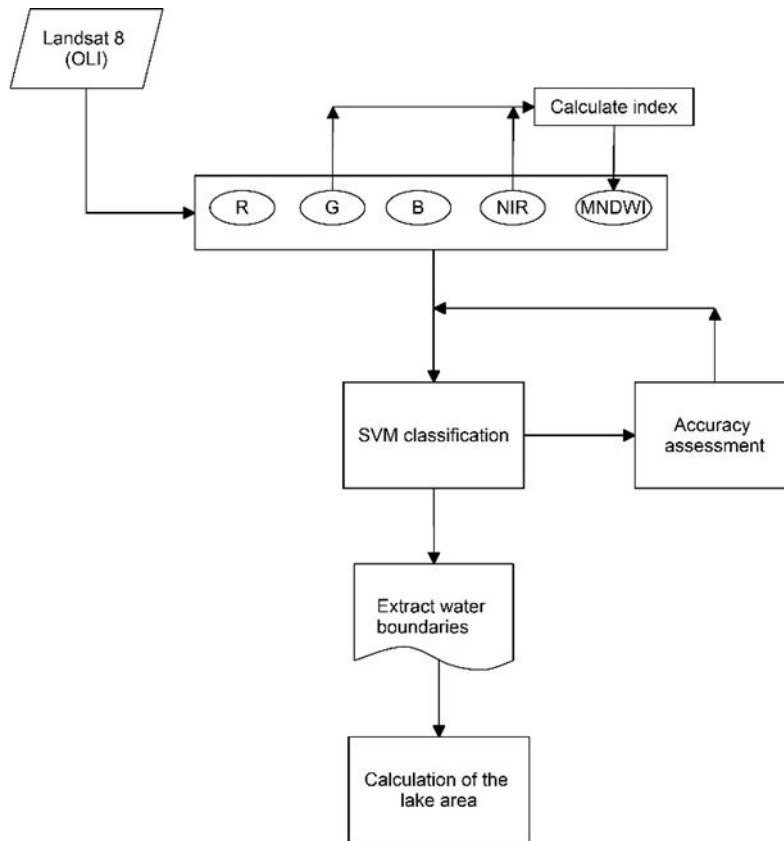


Figure 2. Classification flowchart

2.3.1. Normalized difference water index

In Landsat-8 (OLI) satellite images, the NDWI is the normalized difference between the green band (band 3) and the near-infrared band (band 5). This index distinguishes water surfaces from other details on remotely sensed images. NDWI is widely used in the extraction of water bodies. The NDWI index is calculated by Equation 1.

$$NDWI = \frac{Green - NIR}{Green + NIR} \quad (1)$$

where NIR represents the near-infrared band, and green represents the green band. Water generally takes high NDWI values. NDWI values range from -1 to +1. Values close to +1 and +1 represent water, while values of 0 and below indicate the absence of water [27].

3. Results

In the study, satellite images of different time series (2013-2022) were processed on the GEE platform, and the change in the water surface area of Marmara Lake was examined. The satellite images monitored annual water surface changes with the NDWI index and SVM algorithm used to extract the water surface. When seasonal changes are examined, the average water surface area in 2013 was calculated as 5,297.95 ha. The same area was determined as 1,322.18 ha on average as of January 2022. The lake water surface area detected a decrease of 3,975.78 ha in the mentioned period. This area corresponds to approximately 75% of the surface area calculated in 2013. In other words, most of the Marmara Lake dried up in the specified period. Since the water levels in the spring seasons will be more realistic, this situation is shown in Fig. 3 with the maps of the spring seasons of 2013 and 2021.

Additionally, when seasonal inspections of the lake's water area were conducted, it was determined that the lake reached its maximum size in the spring of 2014 and completely dried up in the fall of 2021. The change in the lake water surface is shown in Figure 3. In Figure 4, the seasonal water surface and average area change graph show that the water surface area continued to average around 5,000 ha between 2013 and 2016, but the average water surface tended to decrease in the following years.

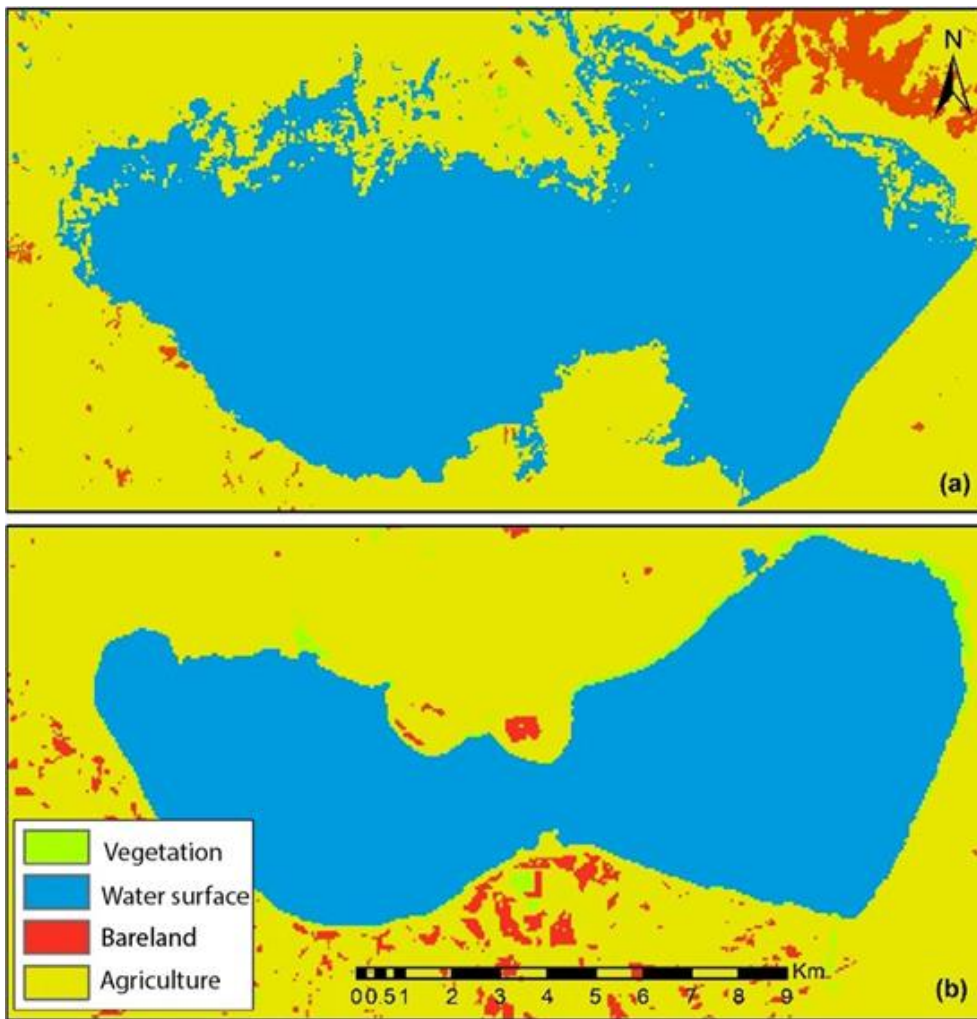


Figure 3. 2013 (a)-2021 (b) spring land change

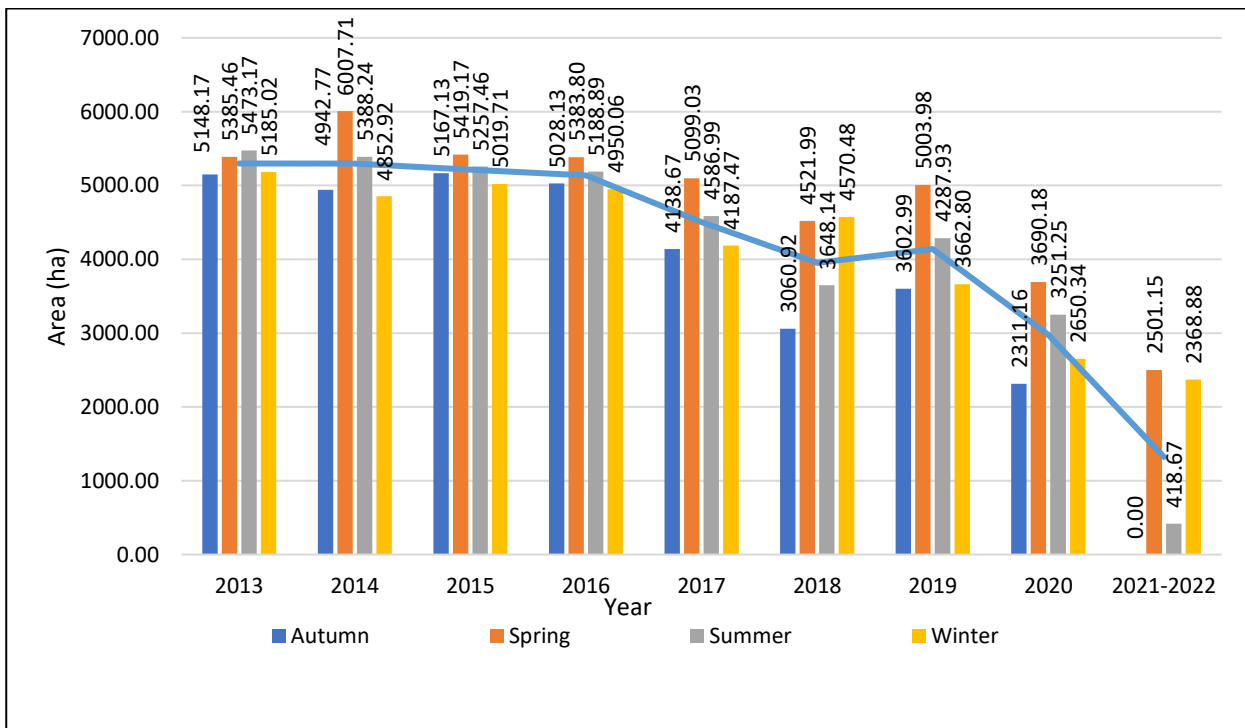


Figure 4. Seasonal change of water surface areas

RS techniques are widely preferred today in the determination of water surfaces. Like this study, Hossen et al. [28] investigated the changes in the surface area of Lake Manzala in Egypt with RS techniques. They applied supervised and unsupervised classification techniques in their study. They also used NDWI to extract the water surface. Their study found that the water surface decreased by 46% between 1984 and 2015. Today, quite common water extraction indexes such as NDWI, MNDWI, and AWEI are used to extract water surfaces. The selection of these indices varies according to the characteristics of the water (dirty water, shallow or deep water, etc.) or environmental effects (urban area, shaded area, open area, etc.). Although the NDWI index was used in this study, MNDWI was used in our research, which gives better results, especially in shallow waters. Yang et al. [29] used MNDWI and AWEI indexes to extract water in urban areas in their study. In this study, it is noteworthy that MNDWI and AWEI were used to separate water from other details, especially in urban areas. The shadow effect on water in urban areas is greater than in open areas. Due to this effect, MNDWI index is more sensitive to spectral differences on water. Chen et al. [30] took into account the seasonal changes of the lake water in their study, as in our study. For this purpose, they estimated the lake water level from satellite altimetry data. Worden and Beurs [31] evaluated their performance using different water extraction indices on Landsat 8 images to detect water surfaces in the Caucasus. In their study, they determined that MNDWI performed better than others. They determined the water surfaces with 93% accuracy. This classification accuracy showed high accuracy, similar to our study.

3.1. Accuracy assessment

The classification accuracy of this study was tested by an error matrix. User's accuracy (UA), producer's accuracy (PA), overall accuracy (OA), and kappa (κ) were calculated in the created error matrix. For this purpose, random polygons were defined for each class on the GEE platform, and the pixels within these polygons were accounted for classification accuracy. Classification accuracy values are given in Table 2.

Table.2 Classification accuracies

	Autumn				Spring				Summer				Winter			
	UA	PA	OA	κ	UA	PA	OA	κ	UA	PA	OA	κ	UA	PA	OA	κ
2013	100.	100.00	89.6	0.75	90.8	93.7	90.0	0.78	87.2	100.	93.7	0.86	81.	100.0	91.0	0.79
2014	100.	100.00	96.8	0.93	79.4	99.8	90.8	0.81	90.0	100.	94.4	0.88	84.	100.0	92.3	0.81
2015	100.	100.00	95.6	0.90	94.4	100.	95.7	0.91	86.4	100.	96.8	0.93	82.	100.0	91.9	0.81
2016	41.0	100.00	86.4	0.71	98.7	100.	93.4	0.87	93.1	100.	96.8	0.93	83.	100.0	93.2	0.84
2017	86.0	100.00	94.7	0.87	100.	100.	95.5	0.91	94.9	100.	94.4	0.87	88.	100.0	92.5	0.81
2018	100.	100.00	91.8	0.79	100.	100.	93.9	0.88	100.	100.	95.7	0.90	81.	100.0	92.4	0.82
2019	99.8	20.19	92.3	0.82	100.	100.	89.0	0.78	100.	100.	93.5	0.85	91.	100.0	91.3	0.79
2020	100.	100.00	94.3	0.85	90.0	100.	93.5	0.84	100.	100.	95.2	0.86	100	100.0	92.0	0.80
2021-	0.00	0.00	91.8	0.71	100.	100.	94.7	0.87	100.	100.	97.0	0.92	99.	100.0	96.2	0.89

Table 2 shows the accuracy values for UA and PA water surfaces. The OA and κ values represent the accuracy assessment of the complete classification. UA and PA values for water surfaces were above 85% in almost all years. Likewise, it was seen that the OA value was classified with an accuracy of nearly 90% over the seasons of all years. Classification accuracy could not be calculated due to water withdrawal in the lake in the 2021 autumn season. According to the classification accuracies calculated in this study, it can be easily said that this classification is successful.

4. Conclusion

In the study, the water surface area changes of Marmara Lake, located within the borders of Manisa province, were examined with GEE, a cloud-based RS platform. The change in the lake's water surface area between 2013-2022 is shown in Fig. 4, and a 75.04% decrease in the water surface area has been detected. In addition, while the amount of agricultural land around the lake was 13,369.39 ha in 2013, this area was determined as 15,100.79 ha in 2021. In other words, the agricultural area around the lake has increased by 12.95%. As shown in Fig. 3, this area was used for agricultural purposes after the water withdrawal from the lake.

As a result, the increased agricultural lands around the lake, unconscious resource use, drought, and evaporation due to global climate change have caused significant lake water surface area changes. Marmara Lake, one of the critical water resources of the Aegean Region, has an important place in terms of biodiversity. To protect such resources, more conscious and sustainable land management plans should be prepared, and it is recommended that these areas be protected.

Funding

This research received no external funding.

Author contributions

Ramazan Gungor: Conceptualization, Methodology, Software **Osman Salih Yilmaz:** Data curation, Writing-Original draft preparation, Software, Validation. **Fusun Balik Sanli and Ali Murat Ates:** Visualization, Investigation, Writing-Reviewing and Editing.

Conflicts of interest

The authors declare no conflicts of interest.

References

1. Duan, W., Maskey, S., Chaffe, P. L., Luo, P., He, B., Wu, Y., & Hou, J. (2021). Recent advancement in remote sensing technology for hydrology analysis and water resources management. *Remote sensing*, 13(6), 1097.
2. Rundquist, D. C., Narumalani, S., & Narayanan, R. M. (2001). A review of wetlands remote sensing and defining new considerations.
3. Díaz-Pinzón, L., Sierra, L., & Trillas, F. (2022). The Economic Value of Wetlands in Urban Areas: The Benefits in a Developing Country. *Sustainability*, 14(14), 8302.
4. Yan, Z., Zhang, K., Peng, Q., Kang, E., Li, M., Zhang, X., ... & Kang, X. (2022). Spatio-Temporal Variations and Socio-Economic Driving Forces for Wetland Area Changes: Insights from 2008–2017 Data of Yunnan Province, China. *Water*, 14(11), 1790.
5. Mitsch, W. J., Gosselink, J. G., Zhang, L., & Anderson, C. J. (2009). *Wetland ecosystems*. John Wiley & Sons.
6. Ouma, Y. O., & Tateishi, R. (2006). A water index for rapid mapping of shoreline changes of five East African Rift Valley lakes: an empirical analysis using Landsat TM and ETM+ data. *International Journal of Remote Sensing*, 27(15), 3153-3181.
7. Verpoorter, C., Kutser, T., & Tranvik, L. (2012). OCEANOGRAPHY: METHODS Automated mapping of water bodies using Landsat multispectral data. 1037–1050
8. Arekhi, M., Goksel, C., Balik Sanli, F., & Senel, G. (2019). Comparative evaluation of the spectral and spatial consistency of Sentinel-2 and Landsat-8 OLI data for Igneada longos forest. *ISPRS International Journal of Geo-Information*, 8(2), 56.
9. Albarqouni, M. M., Yagmur, N., Bektas Balcik, F., & Sekertekin, A. (2022). Assessment of Spatio-Temporal Changes in Water Surface Extents and Lake Surface Temperatures Using Google Earth Engine for Lakes Region, Turkey. *ISPRS International Journal of Geo-Information*, 11(7), 407.
10. Eid, A. N. M., Olatubara, C. O., Ewemoje, T. A., Farouk, H., & El-Hennawy, M. T. (2020). Coastal wetland vegetation features and digital Change Detection Mapping based on remotely sensed imagery: El-Burullus Lake, Egypt. *International Soil and Water Conservation Research*, 8(1), 66-79.
11. Feeters, S. (1996). El Uso del Índice de Agua de Diferencia Normalizada (NDWI) en la Delineación de Características de Aguas Abiertas. *Revista Internacional de Teledetección* (17), 1425-1432.
12. Babaei, H., Janalipour, M., & Tehrani, N. A. (2021). A simple, robust, and automatic approach to extract water body from Landsat images (case study: Lake Urmia, Iran). *Journal of Water and Climate Change*, 12(1), 238-249.
13. Cordeiro, M. C., Martinez, J. M., & Peña-Luque, S. (2021). Automatic water detection from multidimensional hierarchical clustering for Sentinel-2 images and a comparison with Level 2A processors. *Remote Sensing of Environment*, 253, 112209.
14. Rad, A. M., Kreitler, J. R., & Sadegh, M. (2021). Augmented normalized difference water index for improved monitoring of surface water. *Environmental Modeling and Software*, 140.
15. Reis, S., & Yilmaz, H. M. (2008). Temporal monitoring of water level changes in Seyfe Lake using remote sensing. *Hydrological Processes: An International Journal*, 22(22), 4448-4454.
16. Sun, F., Sun, W., Chen, J., & Gong, P. (2012). Comparison and improvement of methods for identifying waterbodies in remotely sensed imagery. *International journal of remote sensing*, 33(21), 6854-6875.
17. Jawak, S. D., & Luis, A. J. (2014). A semiautomatic extraction of Antarctic Lake features using WorldView-2 imagery. *Photogrammetric Engineering & Remote Sensing*, 80(10), 939-952.
18. Temiz, F., Bozdag, A., Durduran, S. S., & Gumus, M. G. (2017). Monitoring coastline change using remote sensing and GIS technology: a case study of Burdur Lake, Turkey. *Fresenius Environmental Bulletin*, 26(12), 7235-7242.

19. Mansaray, L. R., Wang, F., Huang, J., Yang, L., & Kanu, A. S. (2020). Accuracies of support vector machine and random forest in rice mapping with Sentinel-1A, Landsat-8 and Sentinel-2A datasets. *Geocarto International*, 35(10), 1088-1108.
20. Yue, H., Li, Y., Qian, J., & Liu, Y. (2020). A new accuracy evaluation method for water body extraction. *International Journal of Remote Sensing*, 41(19), 7311-7342.
21. Zhuang, Q., Zhang, J., Cheng, L., Chen, H., Song, Y., Chen, S., ... & Li, M. (2022). Framework for Automatic Coral Reef Extraction Using Sentinel-2 Image Time Series. *Marine Geodesy*, 45(3), 195-231.
22. Robinson, N. P., Allred, B. W., Jones, M. O., Moreno, A., Kimball, J. S., Naugle, D. E., ... & Richardson, A. D. (2017). A dynamic Landsat derived normalized difference vegetation index (NDVI) product for the conterminous United States. *Remote sensing*, 9(8), 863.
23. Patel, N. N., Angiuli, E., Gamba, P., Gaughan, A., Lisini, G., Stevens, F. R., ... & Trianni, G. (2015). Multitemporal settlement and population mapping from Landsat using Google Earth Engine. *International Journal of Applied Earth Observation and Geoinformation*, 35, 199-208.
24. Goldblatt, R., You, W., Hanson, G., & Khandelwal, A. K. (2016). Detecting the boundaries of urban areas in india: A dataset for pixel-based image classification in google earth engine. *Remote Sensing*, 8(8), 634.
25. Gülersoy, A. (2013). Marmara Gölü yakın çevresindeki arazi kullanım faaliyetlerinin zamansal değişimi (1975-2011) ve göl ekosistemlerine etkileri. *Türk Coğrafya Dergisi*, (61), 31-44.
26. <https://kulasalihligeopark.com/marmara-golu/>
27. Kaplan, G., & Avdan, U. (2017). Water extraction technique in mountainous areas from satellite images. *Journal of Applied Remote Sensing*, 11(4), 046002.
28. Hossen, H., Ibrahim, M. G., Mahmud, W. E., Negm, A., Nadaoka, K., & Saavedra, O. (2018). Forecasting future changes in Manzala Lake surface area by considering variations in land use and land cover using remote sensing approach. *Arabian Journal of Geosciences*, 11(5), 1-17.
29. Yang, X., Qin, Q., Grussenmeyer, P., & Koehl, M. (2018). Urban surface water body detection with suppressed built-up noise based on water indices from Sentinel-2 MSI imagery. *Remote sensing of environment*, 219, 259-270.
30. Chen, T., Song, C., Ke, L., Wang, J., Liu, K., & Wu, Q. (2021). Estimating seasonal water budgets in global lakes by using multi-source remote sensing measurements. *Journal of Hydrology*, 593, 125781.
31. Worden, J., & de Beurs, K. M. (2020). Surface water detection in the Caucasus. *International Journal of Applied Earth Observation and Geoinformation*, 91, 102159.



© Author(s) 2022. This work is distributed under <https://creativecommons.org/licenses/by-sa/4.0/>



Advanced Remote Sensing

<http://publish.mersin.edu.tr/index.php/arcej>

e-ISSN 2979-9104



Determination of city change in satellite images with deep learning structures

Mustafa Emre Dos*¹ 

¹ Hatay Mustafa Kemal University, Department of Architecture and Urban Planning, Hatay, Türkiye, mustafaemre.dos@mku.edu.tr

Cite this study: Dos, M. E. (2022). Determination of city change in satellite images with deep learning structures. *Advanced Remote Sensing*, 2(1), 16-22

Keywords

Remote Sensing
Deep Learning
Classification
Change Detection

Research Article

Received: 23.05.2022
Revised: 19.06.2022
Accepted: 24.06.2022
Published: 30.06.2022

Abstract

Uneven urban growth is a major problem worldwide as it causes serious losses in vital areas such as farmland and water bodies. In this context, the management of the factors such as agriculture, industry, housing, etc. of the cities as a whole and the studies carried out for the planning should be followed in real life. Change detection based on remote sensing images plays an important role in the field of remote sensing analysis and is widely used in many areas such as resource monitoring, urban planning, disaster assessment, etc. However, the detection of changes in the same areas from satellite images at different times makes it difficult to interpret and detect them with human capabilities due to their dense information content. Recently, with the developments in computer vision technology, deep learning structures have come to the fore in the interpretation of satellite data. In this study, using the Onera Satellite Change Detection (OSCD) data set, change detection from satellite images of different dates belonging to the same regions was tried to be extracted with deep learning structures.

1. Introduction

With the increasing amount of population in the world and in our country, limited resources should be used effectively and correctly. Effective resource utilization can be achieved by using appropriate statistical information of regions such as building density, industrialization rate, road network indicators, proportion of informal settlements in the region and others in urbanization models. These parameters can be applied to develop future urban growth scenarios and use them in the decision-making process [1-3]. In the creation of regular urbanization models, remote sensing data are frequently used today thanks to the monitoring of large areas and the data provided in different spectral bands [4,5]. At the same time, for the real-life monitoring of these models, change detection can be made thanks to the temporal series of remote sensing data. Today, there are many details in the images of objects used in remote sensing. Because of this density of detail, classifying and then interpreting this data is just as important as obtaining the data. However, detecting changes from what is given remote sensing is a challenging task due to the complexity of dimensions and details.

Deep learning structures have recently become popular again thanks to the powerful solutions they offer in many areas [6-9]. In this context, it is a powerful alternative to the problem of detail confusion caused by the large size of the remote sensing data for change detection. Before the prevalence of deep learning, the problem of change detection was mainly solved by handmade features derived from complex feature extractors. The poor expressibility of features extracted by traditional methods significantly reduces the accuracy of change detection and is sensitive to the effects of factors such as seasonal change, lighting conditions, satellite sensors, and solar altitude angle. In general, traditional methods that require expert knowledge are typically not optimal, and

empirical features are poor at representing images [10]. Unlike traditional methods, deep learning methods extract features from images in spectral and semantic relationships, thereby bringing high accuracy and automation. Thanks to these innovative features, deep learning structures are seen as a good alternative to the problem of change detection in remote sensing. However, pixel-wise annotated change detection datasets are available that can be used to train supervised machine learning systems that detect changes in image pairs, such as the Onera Satellite Change Detection (OSCD) dataset and Air Change dataset [11].

Previous studies are based on statistical estimation methods and classical machine learning methods such as the support vector machine [12]. In later studies, convolutional neural networks (CNNs) have been proposed to detect the difference between two images using patch images [13]. Daudt et al. [14] introduced two Siamese extensions of fully convolutional networks trained from scratch to end, leaving behind the latest technology for change detection in both accuracy and inference speed without the need for finishing. Notable among these modifications is the transformation of the fully convolutional encoder-decoder paradigm into a Siamese architecture that uses hop links to improve the spatial accuracy of outputs. Jaturapitpornchai et al. [15] proposed in detail a U-Net-based network that detects new building construction in developing regions using two SAR images captured at different times. Later, the U-Net architecture was expanded with a few changes in other works. Hamdi et al. [16] ArcGIS has developed an algorithm using a modified U-Net model for automatic detection and mapping of damaged areas in the environment. The study areas were trained based on a database of a forest area in Germany. Khusni et al. [17] proposed a method that combined a BiLSTM structure with a CNN structure based on Unet [18]. The proposed architecture first infers features with the CNN structure and keeps the extracted feature in memory with the BiLSTM structure and predicts whether there has been a change as a result product. A high accuracy was achieved in this study, but the process complexity is many. Lin, Y. et al. [19] proposed a two-sided convolution network to detect changes in bitemporal multispectral images. They trained the model with two symmetrical CNNs that could learn feature representations. They applied the outer matrix product to the output feature maps to obtain combined known properties. The Softmax classifier was applied to produce the detected change results. Zhang et al. [20] proposed a new FDCNN-based CD approach, in which sub-VGG16 was used to learn deep features from remote sensing images, FD-Net was used to create feature difference maps, and FF-Net was used to combine these maps by training with a small number of pixel-level samples. However, the network is not easily applicable because high pixel resolution samples are desired.

In many remote sensing applications, remembering the necessary training data and rebuilding models is too expensive or impossible. Transfer learning is defined as the ability to extract information from one or more source tasks and apply it to a new or target task [21]. Venugopal et al. [22] they resorted to a ResNet-101[23] network as a pre-trained model and fine-tuned the parameters based on an enlarged convolutional neural network that detected changes between the two images. Then, the classified result is determined as unchanged and changed areas from the final feature map. Fang et al. [24] He proposed a new hybrid end-to-end framework called the binary learning-based s edge framework (DLSF) for change detection from very high resolution (VHR) images. This framework consists of two parallel flows, binary learning-based domain transfer and Siamese-based exchange decision. The first way aims to reduce the domain differences between the two paired images and preserve the internal information by translating it into each other's domain, while the second way aims to learn a decision strategy to decide on changes in the two areas respectively.

Deep learning methods have come to the agenda again with the development of technology. However, with the developing technology, the hardware and software requirements needed have increased and the costs have increased. Due to rising costs, the advantages of remote sensing platforms cannot be fully emphasized. Cloud systems have come to the agenda as a solution to these reasons. Large companies such as Google and Amazon provide their users with great hardware advantages thanks to cloud systems.

When the literature is examined, a general solution for the problem of change detection cannot be presented. Within the scope of this study, the performance of deep learning methods for the problem of change detection from remote sensing data was evaluated and in the light of the results obtained, it was tried to pioneer future studies. In the deep learning method selected for this study, unlike the transfer learning method, end-to-end training was performed from the ready-made data set, and it was tried to get rid of heavy initial values and feature learning of different areas. Another aim of this study was to use a cloud system as an alternative to desktop computers that require high-cost hardware requirements that allow the use of deep learning structures, and its performance was evaluated.

2. Material and Method

In this study, the architecture based on Unet, which has little complexity and can learn to perceive changes only from change-perceptive datasets without transferring any pre-training or learning from other datasets, is used for change detection [12]. The architecture used is shown in Figure 1. Thanks to the easy use developed by Google, the Pytoch library was used as a library. A proposed pre-labeled dataset for OSCD change detection was used as the data set. Google Colab cloud system was selected as the working environment and Graphic Process Unit (GPU) and Central Process Unit (CPU) systems offered were compared. Tesla T4 was used by the GPU.

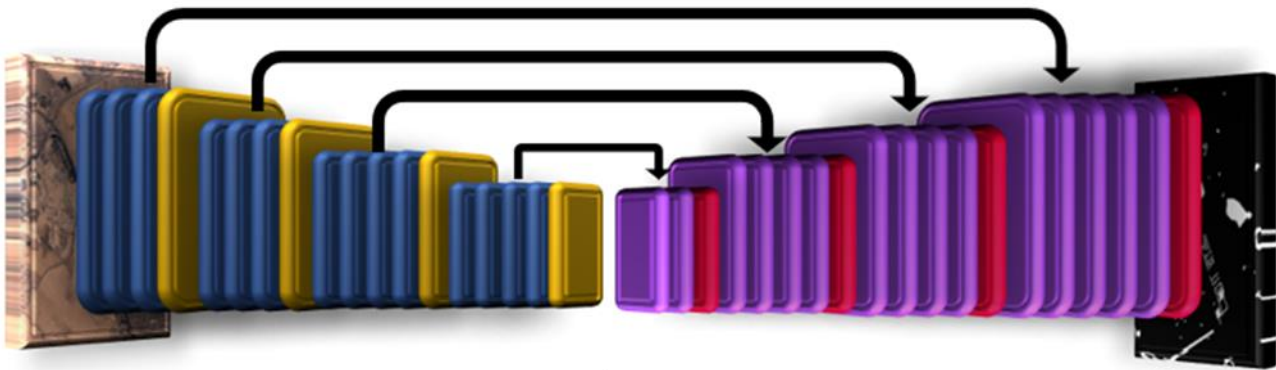


Figure 1. Schematic of the proposed architecture for urban change detection. Block color legend: blue is ReLu+convolutional, yellow is max pooling, res is concatenation, purple is transpose convolutional

2.1. Deep Learning Architecture

In this study, the Early Fusion (EF) architecture presented in [8] was used. In architecture, patch images are output at 96x96 sizes. The EF architecture takes two image patches from different dates and combines them before migrating them to the network, treating them as different color channels. The proposed architecture is based directly on the Unet model and is referred to as Fully Convolutional Early Fusion (FC-EF). Thanks to the convolutional layers in the architecture, it learns the low, medium and high characteristics from the given image, as in Figure 2. It includes only four maximum pooling and four supersampling layers instead of five layers to prevent overfitting after convolutional layers. The tiers in FC-EF are also shallower than their U-Net equivalents. Finally, the architecture departs from the softmax layer and classifies the entire image as to whether there has been a change or no change.

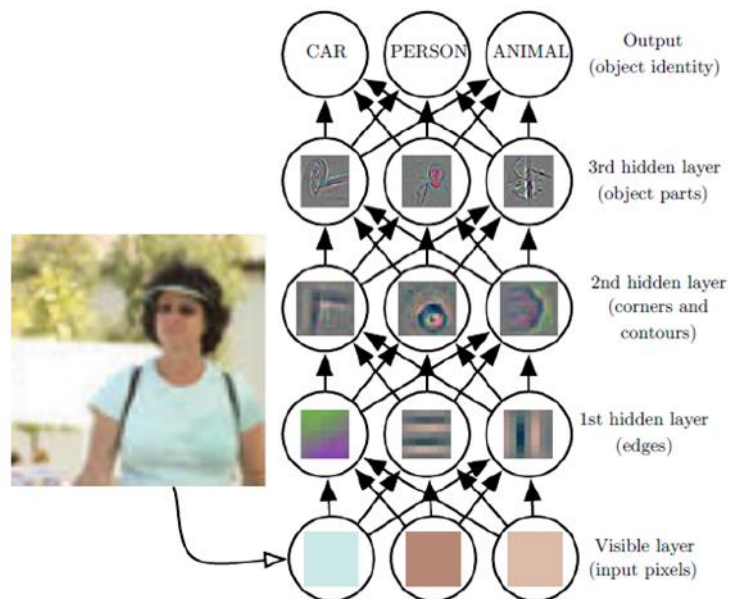


Figure 2. How to convolutional layers extraction to feature from given image [25]

2.2. Dataset

OSCD dataset addresses the issue of detecting changes between satellite images from different dates. It comprises 24 pairs of multispectral images taken from the Sentinel-2 satellites between 2015 and 2018. Locations are picked all over the world, in Brazil, USA, Europe, Middle East and Asia. For each location, registered pairs of 13 band multispectral satellite images obtained by the Sentinel-2 satellites are provided. Images vary in spatial resolution between 10m, 20m and 60m. Pixel-level change ground truth is provided for all 14 training and 10 test image pairs. The annotated changes focus on urban changes, such as new building or new roads. These data can be used for training and setting parameters of change detection algorithms.

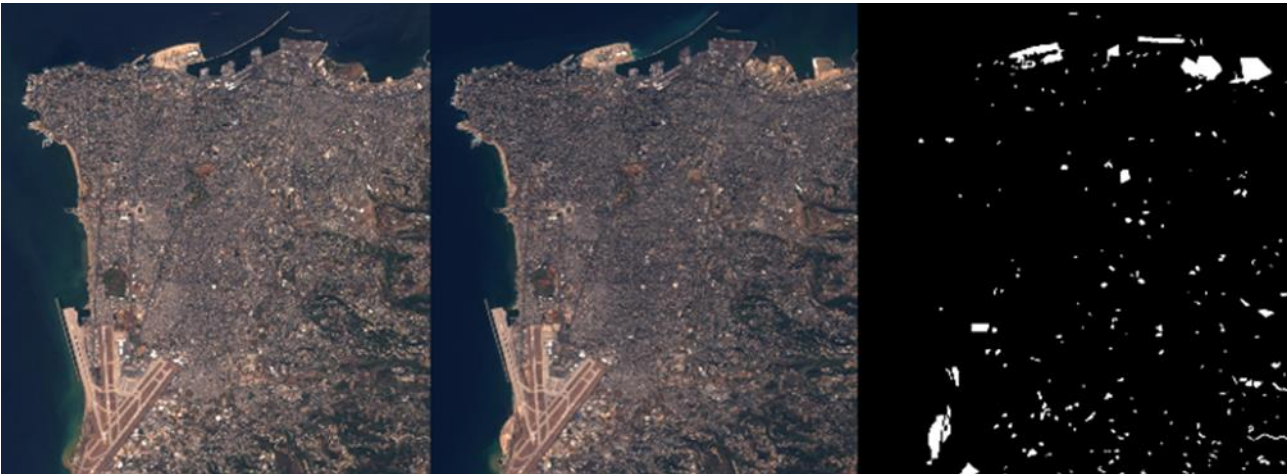


Figure 3. From left to right: image from 2015, image from 2018 and labelling change image

3. Results

All stages of the training were carried out in the Google Colab cloud environment. The training and testing phase with the Google Colab GPU lasted 3.5 hours. The training and testing phase with the Google Colab CPU lasted approximately 5.5 hours. The general accuracy and loss values of the training and testing phases performed in both environments are presented in Table 1. The results obtained from the Google Colab GPU and CPU at the end of the test phase are presented in Figure 4. In the images given as GPU and CPU outputs shown in the Fig. 4, the pink pixels are labeled as the places where the algorithm predicts correctly, the white pixels are the places that the algorithm cannot predict but the places that the algorithm cannot predict, and the green parts are labeled as the places where the algorithm predicts the change as not changing.

Table 1. Results obtained as a result of training as GPU and CPU

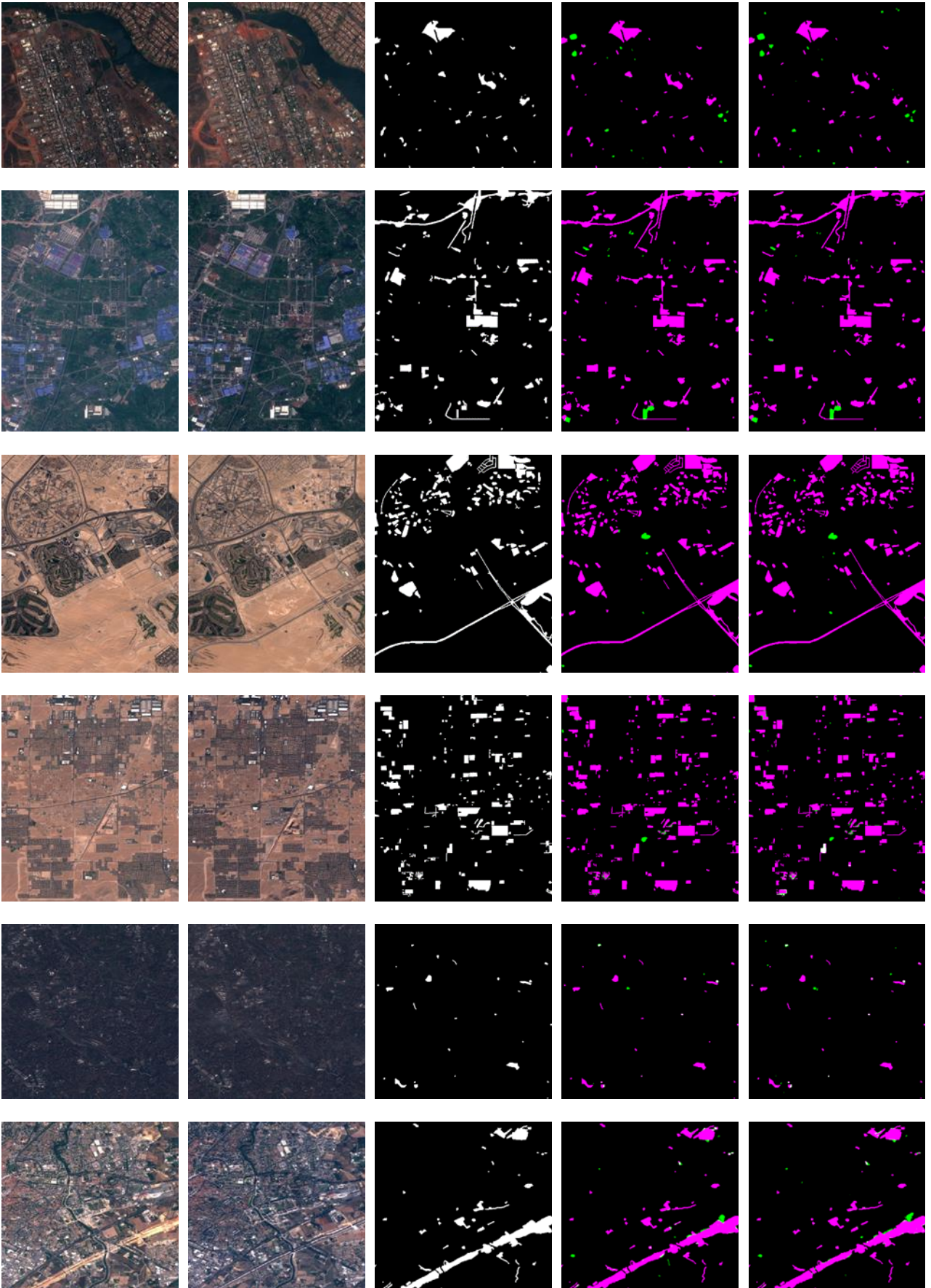
Items	Total Accuracy (%)	Total Loss
GPU	94,72	0,1132
CPU	90,59	0,2134

4. Discussion

As a result of the study, it was seen that the experiment with the GPU gave better results when the general accuracy was considered, but there were no large result differences between the GPU and the CPU. In temporal performance, the Tesla T4 GPU system, which was used as expected, performed almost twice as well as the Google Colab CPU. However, considering that Google Colab offers 12 hours of GPU support, it seems that the Google Colab CPU will be enough unless there are very demanding tasks.

When the output images obtained as a result of the test process are examined, it is seen that the proposed deep learning architecture has achieved a good accuracy in general. The green pixels in the output images are regions where there is no change, but which the architecture perceives as a change. When the areas where green regions are concentrated are examined, the algorithm estimated that the reflection values changed in these areas, but it was seen that there were differences in the reflection value instead of the change in agricultural areas and building roofs. The white areas in the output images are different places where the algorithm cannot detect changes. When white areas are examined, it is thought that the algorithm loses its contextual continuity due to low pixel resolution.

In the light of the results obtained, high accuracy has been achieved in the resulting products thanks to the advantages of CNN-based deep learning architectures such as automatic extraction of features from remote sensing data, unlike classical machine learning methods for change detection. In addition to statistical relationships from remote sensing images of classical methods such as support vector machines, the learning process was used more effectively thanks to semantic relationships. The deep learning architecture used was trained from scratch end-to-end with the OSCD dataset and no initial weight was taken. In this way, as in transfer learning methods, output products independent of the semantic differences of the weights previously trained with different data sets were obtained.



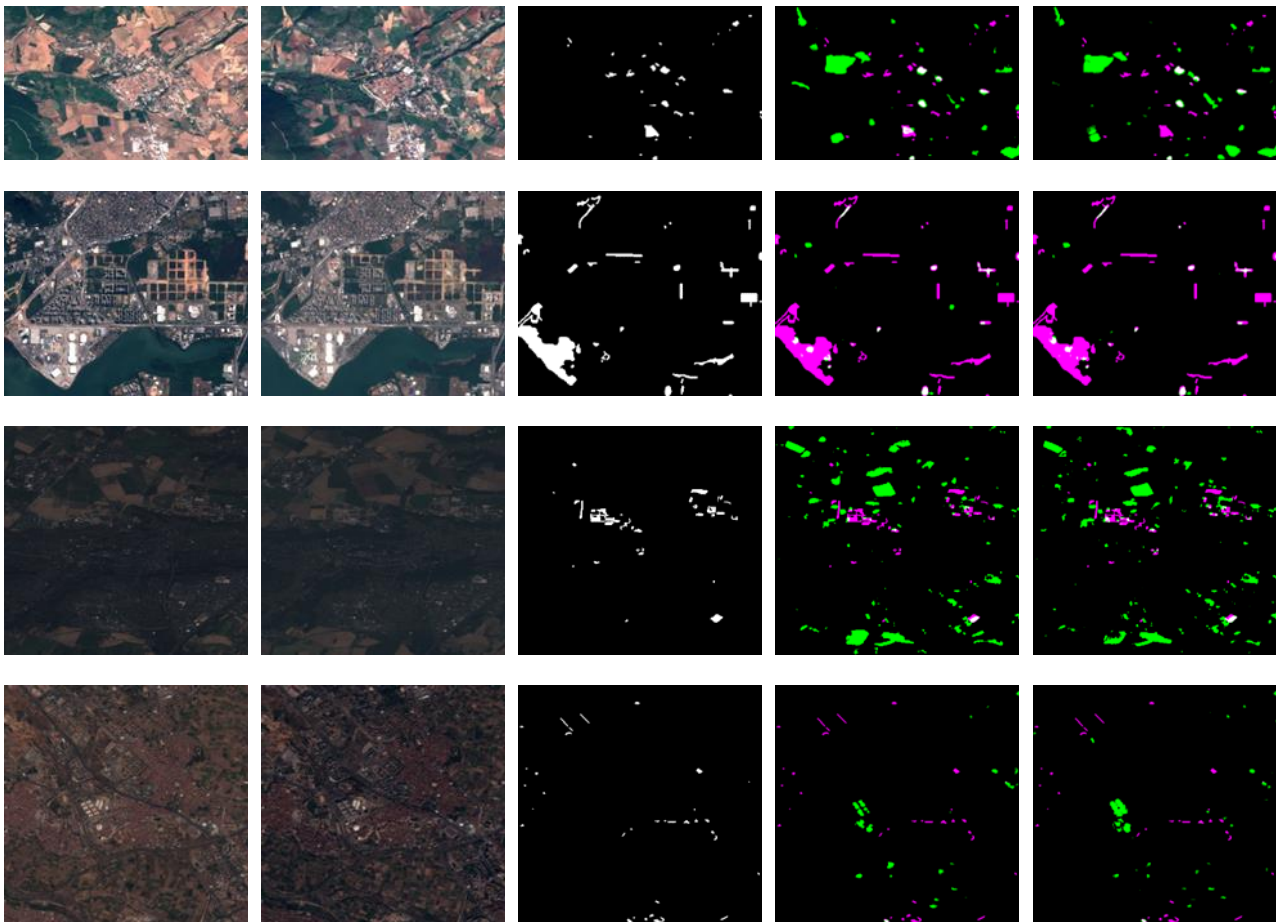


Figure 4. From left to right: image from 2015, image from 2018, labelling change image, output of GPU and output of CPU

5. Conclusion

In this study, deep learning algorithms were tested as software architecture and Google Colab cloud system as hardware deficiency for change detection problem. In the light of the results obtained, deep learning algorithms have achieved high accuracy in contrast to previous classical machine learning methods and have shown that there is a good alternative solution. It is necessary to have high processing power in order to run deep learning algorithms. In order to reduce the cost of this vulnerability, the performance of the Google Colab cloud environment has been evaluated and it is thought that this problem can be overcome when the results are examined. The biggest problem with deep learning architectures is still the lack of a data set with label images covering all areas. If deep learning architectures are to be preferred for the detection of differences, instead of making a total inference, it is thought that it will be healthier to examine issues such as the extraction of details such as buildings, roads, trees, etc. in terms of the effectiveness of deep learning architectures in contextual inferences.

Funding

This research received no external funding.

Conflicts of interest

The authors declare no conflicts of interest.

References

1. Dadashpoor, H., Azizi, P. & Moghadasi, M. (2019). Analyzing spatial patterns, driving forces, and predicting future growth scenarios for supporting sustainable urban growth: Evidence from Tabriz metropolitan area. *Sustainable Cities and Society*, 47, 101502.
2. Liang, X., Liu, X., Li, D., Zhao, H. & Chen, G. (2018). Urban growth simulation by incorporating planning policies into a CA-based future land use simulation model. *International Journal of Geographical Information Science*, 32(11), 2294-2316.
3. Serasinghe, P.I.S., Kantakumar, L. N. & Sundaramoorthy, S. (2018). Remote sensing data and SLEUTH urban growth model: Decision support tools for urban planning *Chinese Geographical Science* 28, 274-286.
4. Zhang, Z., Vosselman, G., Gerke, M., Tuia, D., Yang, M.Y. (2018). Change detection between multimodal remote sensing data using siamese CNN. arXiv 2018, arXiv:1807.09562.
5. Chen, J., Liu, H., Hou, J., Yang, M., & Deng, M. (2018). Improving building change detection in VHR remote sensing imagery by combining coarse location and co-segmentation. *ISPRS International Journal of Geo-Information*, 7(6), 213.
6. Xu, X., Li, W., Ran, Q., Gao, L., Zhang, B. (2018). Multisource remote sensing data classification based on convolutional neural network. *IEEE Transactions on Geoscience and Remote Sensing*, 56(2), 937-949
7. Li, Y., Zhang, H., Xue, X., Jiang, Y., Shen, Q. (2018). Deep learning for remote sensing image classification: a survey. *Wiley Interdisciplinary Reviews Data Mining and Knowledge Discovery*, 8, e1264
8. Deng, Z., Sun, H., Zhou, S., Zhao, J., Lei, L., Zou, H. (2018). Multi-scale object detection in remote sensing imagery with convolutional neural networks. *ISPRS Journal of Photogrammetry and Remote Sensing*, 145, 3-22.
9. Zhang, Z., Jiang, R., Mei, S., Zhang, S., Zhang, Y. (2020). Rotation-Invariant feature learning for object detection in VHR optical remote sensing images by Double-Net. *IEEE Access*, 8, 20818-20827.
10. Jiang, H., Peng, M., Zhong, Y., Xie, H., Hao, Z., Lin, J., Ma, X., Hu., X. (2022). A survey on deep learning-based change detection from high-resolution remote sensing images. *Remote Sensing*, 14(7), 1552.
11. Benedek, C. & Sziranyi, T. (2009). Change detection in optical aerial images by a multilayer conditional mixed markov model. *IEEE Transaction on Geoscience and Remote Sensing*, 47(10), 3416-3430.
12. Martins, S., Bernardo, N., Ogashawara, I. & Alcantara, E. (2016) Support vector machine algorithm optimal parameterization for change detection mapping in funil hydroelectric reservoir (Rio de Janeiro State, Brazil). *Modeling Earth Systems and Environment*, 2, 138.
13. Zagoruyko, S. & Komodakis, N. (2015) Learning to compare image patches via convolutional neural networks. *IEEE Conference on Computer Vision and Pattern Recognition (CVPR)*, Boston, MA, USA.
14. Daudt, R. C., Le Saux, B. & Boulch, A. (2018) Fully convolutional siamese networks for change detection. *IEEE International Conference on Image Processing (ICIP)*, 4063-4067, Athens, Greece.
15. Jaturapitpornchai, R., Matsouka, M., Kanemoto, N., Kuzuoka, S., Ito, R., Nakamura, R. (2019) Newly built construction detection in SAR images using deep learning. *Remote Sensing*, 11(12), 1-24.
16. Hamdi, Z.M., Brandmeier M. & Straub, C. (2019) Forest damage assessment using deep learning on high resolution remote sensing data. *Remote Sensing*, 11(17), 1976.
17. Khusni, U., Dewangkoro, I. H. & Arymurthy, M. A. (2020) Urban area change detection with combining CNN and RNN from sentinel-2 multispectral remote sensing data. *3rd International Conference on Computer and Informatics Engineering (IC2IE)*, Yogyakarta, Indonesia.
18. Ronneberger, O., Fischer, P. & Brox, T. (2015) U-Net: convolutional networks for biomedical image segmentation. *Medical Image Computing and Computer-Assisted Intervention (MICCAI)*, 234-241. Munich, Germany.
19. Lin, Y., Li, S., Fang, L. & Ghamasi, P. (2019) Multispectral change detection with bilinear convolutional neural networks. *IEEE Geoscience and Remote Sensing Letters*, 17(10), 1757-1761.
20. Zhang, M. & Wenzhong, S. (2020) A feature difference convolutional neural network-based change detection method. *IEEE Transactions on Geoscience and Remote Sensing*, 58(10), 7232-7246.
21. Jialin Pan, S. & Yang, Q. (2010) A survey on transfer learning. *IEEE Transactions on Knowledge and Data Engineering*, 22(10), 1345-1359.
22. Venugopal, N. (2019). Sample selection based change detection with dilated network learning in remote sensing images. *Sensing and Imaging*, 20(1), 1-22.
23. He, K., Zhang, X., Ren, S., & Sun, J. (2016). Deep residual learning for image recognition. In *Proceedings of the IEEE conference on computer vision and pattern recognition* (pp. 770-778).
24. Fang, B., Pan, L., & Kou, R. (2019). Dual learning-based siamese framework for change detection using bi-temporal VHR optical remote sensing images. *Remote Sensing*, 11(11), 1292.
25. Goodfellow, I., Bengio, Y., & Courville, A. (2016). *Deep learning (adaptive computation and machine learning series)*. MIT Press. ISBN-10: 0262035613.





Integration of Sentinel-1 and Landsat-8 images for crop detection: The case study of Manisa, Turkey

Muslum Altun ^{*1}, Mustafa Turker ¹

¹Hacettepe University, Department of Geomatics Engineering, Türkiye, altunmuslum06@gmail.com, mturker@hacettepe.edu.tr

Cite this study: Altun, M., & Turker, M. (Year). Integration of Sentinel-1 and Landsat-8 images for crop detection: The case study of Manisa, Turkey. *Advanced Remote Sensing*, 2(1), 23-33

Keywords

SAR and Optical Image
Classification
Crop Detection
Random Forest (RF)
Image Fusion

Research Article

Received: 24.05.2022
Revised: 20.06.2022
Accepted: 25.06.2022
Published: 30.06.2022

Abstract

In this study, the accuracy performance of crop detection through classification was investigated in the integration of Sentinel-1 Vertical-Vertical (VV) and Vertical-Horizontal (VH) polarized Synthetic Aperture Radar (SAR) and Landsat-8 satellite images belonging to a single date. A study area was selected from a region with dense agricultural lands within the boundaries of Manisa, Turkey. Wheat, Tomato, Corn, Corn_2, Cotton, Grapes, Clover and Olive Trees were determined as the crop types. Feature level integration was used to generate image stack and random forest (RF) machine learning algorithm was used for image classification. Classification was carried out using only Sentinel-1 SAR data, only Landsat-8 optical data and the merged data set of Sentinel-1 VV+VH and Landsat 8. Image stacking of Sentinel-1 VV+VH and Landsat 8 increased the classification accuracy. The highest overall accuracy (81.46%) was achieved through classification based on the stacked dataset of the Sentinel-1 VV+VH bands and the Landsat-8 optical bands. The study has shown that the stacked dataset of Sentinel-1 VV+VH and Landsat-8 belonging to a single date has great potential in extracting summer crop types.

1. Introduction

One of the most common uses of earth observation satellites is the detection of agricultural products [1-2]. The information provided by thematic maps obtained from satellite images is very useful for the effective management, monitoring, decision making and computing the statistics of the crops produced in agricultural areas [3-4].

Remote sensing applications in agriculture are performed using the optical and Synthetic Aperture Radar (SAR) images [5-6]. Crop detection is among the most common uses of satellite images in agricultural areas. Although significant progress has been made in classification and crop detection using the optical satellite images, it is not always possible to find images of the desired dates and therefore to extract the necessary information due to constraints, such as cloud cover and temporal resolution. Unlike optical satellites, SAR satellites employ active sensors that provide their own energy for image acquisition. Among the important advantages of SAR satellites are that they are not affected by the weather conditions and have the ability to receive images day and night. For this reason, the use of radar images in the detection of crop types in agricultural areas is becoming more common day by day.

Due to various limiting effects, the combined use of optical and SAR satellite data sets has become inevitable. Their combined use, which is prominent in distinguishing different crop types, increases the interest in agricultural studies [7]. Many studies have been conducted to classify agricultural areas and detect agricultural crops from satellites with different sensors [8-9].

Remote sensing data acquisition is very expensive in terms of time and cost analysis. In this respect, the availability of Sentinel and Landsat satellite images free of charge is very important as they eliminate this difficulty. In addition, Landsat-8 satellite stands out with its wide use in many different areas in terms of its rich band number, providing images with different spatial resolutions to users, and low temporal resolution feature of Sentinel-1 satellite enables images to be used in a short time. With these features, agriculture has become one of the most common usage areas of Sentinel-1 and Landsat-8 images. The use of Sentinel-1 images is of particular importance for crop pattern detection in regions where it is difficult to obtain clear optical images or where a sufficient number of images cannot be obtained [8-11].

Based on the literature search on the related subject, [12] fused the Sentinel-1 SAR image dated April 15, 2018 and April 22, 2018 and Landsat-8 OLI bands dated April 26, 2018 using Decision Level Fusion (DLF) technique and performed classification using the Support Vector Machines (SVM) algorithm. In their study, SAR VV+VH polarized bands were used. The effect of the speckle filter on the results was also measured in the study. In the classification performed using the bands fused with DLF technique without applying a speckle filter, 96.02% overall accuracy and 0.9515 kappa coefficient were obtained. It was observed that the speckle filter reduces the classification accuracy and texture properties produced from the VH polarized band outperformed those produced from VV polarized band.

In the study of [13], resolution merge and The Local Mean Variance Matching (LMVM) data fusion techniques were compared using the Sentinel-1 SAR image dated February 25, 2015 and the Landsat-8 OLI image dated March 18, 2015. As the images, the VV and VH polarized bands of Sentinel-1A were used. Four datasets, Sentinel-1A SAR, Landsat-8 OLI, Resolution merge (Sentinel-1 + Landsat 8) and LMVM (Sentinel-1 + Landsat 8), were used in classification performed using the Maximum Likelihood (ML) algorithm. Based on the results obtained, 58.50% overall accuracy and 0.48 kappa coefficient were calculated when using only Sentinel-1A SAR data, 67.16% overall accuracy and 0.59 kappa coefficient accuracy values were calculated when using only Landsat 8 OLI data, and 79.75% overall accuracy and 0.75 kappa coefficient values were calculated when using the fused data set of Sentinel-1 and Landsat-8 based on resolution merge. In the classification performed using Sentinel 1 + Landsat 8 data fused with the LMVM technique, 59.84% overall accuracy and 0.52 kappa coefficient values were calculated.

In the study of [14], 2.75 m resolution TerraSAR-X and 30 m resolution Landsat ETM+ images were fused using high pass filtering (HPF), Principal Component Analysis with band substitution (PCA) and Principal Component with Wavelet Transform (WPCA) image fusion techniques. Then, the fused images were classified by the decision tree algorithm. Overall accuracy of 74.99%, 83.12% and 85.38%, respectively, and kappa coefficient values of 0.7220, 0.8100, and 0.8369 were obtained from the fused images based on HPF, PCA and WPCA techniques. It was stated that WPCA is the most suitable one among the fusion techniques used.

In the study of [15], Landsat 8 and Sentinel-1 SAR image were fused with the RGB Transformation and Brovey Transformation methods, and their morphology was extracted to sharpen the appearance of lava flow deposits in volcanoes. Sentinel-1 VV polarized band was used in the study. The results were visually analyzed by comparing with the figures. According to the results, the images and techniques used showed that the volcanoes can be observed continuously in all weather conditions.

In the study of [16], Sentinel-1 SAR and Landsat 8 OLI images were fused with the Wavelet, Ehlers, Principal Component Analysis (PCA) and Gram-Schmidt (GS) methods to distinguish summer crop areas, garden areas and orchard areas in the Fergana Valley, Uzbekistan. Images fused with each method were classified using the SVM, Nearest Neighborhood (NN), Random Forest (RF) and Naive Bayesian (NB) algorithms. Classification using RF algorithm on the data set obtained through fusing with the Ehlers method gave the highest overall accuracy of 85.9%.

In the study of [17], paddy crops were detected using the classification of the Normalized Difference Vegetation Index (NDVI) bands derived from Sentinel-1 SAR and Landsat 7 Enhance Thematic Mapper-Plus (ETM+) and Landsat 8 OLI images in Heilongjiang, China. In their study, SAR VV and VH bands and NDVI bands were used together by means of fusing them. The classification was performed using the SVM and RF algorithms. Classification of SAR data in the VH polarized state based on RF algorithm provided the best results with an overall accuracy of 0.94 and a kappa coefficient of 0.93.

In the study of [18], classification was carried out using the RF algorithm on the fused 12 Sentinel-1A, -1B SAR and Landsat-8 data collected at different times in 2015 and 2016 in Sub-Saharan Africa, inside and outside the residential areas. The VV and VH polarization bands of the SAR data were used. It was stated that the VV polarization band performed better than VH. Texture features were created and analyzed with Gray Level Co Occurrence Matrix (GLCM) in different window sizes. Optical and SAR data were combined using PCA image fusion technique. Optical data only, SAR data only, and the fused SAR and optical data were classified using pixel-based RF algorithm. It was stated that classification performed on the fused images provided quite high performance compared to the others.

In the study of [19], image classification was performed to find the best land weave in the Pearl River Delta (PRD) region of China. In their study, the fusion was carried out between the 30 m resolution Landsat ETM+ and 75 m resolution ENVISAT ASAR (WSM) image; 10 m resolution SPOT-5 and 12.5 m resolution ENVISAT ASAR (IMP) image; 10 m resolution SPOT-5 and 3 m resolution TerraSAR-X image. Image fusion was performed using the Pixel

and VH polarized SAR C bands and the Landsat-8 Coastal Aerosol, Blue, Green, Red, Near Infrared, Short-Wave Infrared 1 and Short-Wave Infrared 2 optical bands are given in Table 1.

Table 1. Bands and spatial resolutions of Sentinel-1 and Landsat-8 images

Satellite	Band	Spatial Resolution (m)
Sentinel-1	C band - VV polarization	10
	C band - VH polarization	10
	Band 1 - Coastal Aerosol	30
	Band 2 - Blue	30
	Band 3 - Green	30
Landsat-8	Band 4 - Red	30
	Band 5 - NIR	30
	Band 6 - SWIR 1	30
	Band 7 - SWIR 2	30

Farmer Registration System (FRS) is an agricultural database which contains information about the farmers to ensure that agricultural supports can be monitored, audited, reported and questioned [22]. In this study, we used the existing FRS data as the ground truth reference data. While the spatial information of the FRS data includes the location information, the attribute information consists of land registry information such as, province name, district name, parcel ID, parcel area, cultivated area, cultivated crop types, etc.

3. Methodology

The flowchart summarizing the steps of the method is shown in Figure 2. The method consists of four main steps: data preprocessing, image integration, classification and accuracy analysis. First, the necessary preprocessing steps were applied to Sentinel-1 SAR and Landsat-8 optical images. Then, the necessary arrangements were made on the FRS data so that it can be used as ground reference data. In the second step, feature level integration between Sentinel 1 SAR and Landsat-8 optical images was performed through image stacking. Parcel-based classification of the stacked image dataset was then carried out using the RF machine learning algorithm. As the final step, accuracy assessment of the obtained results was performed.

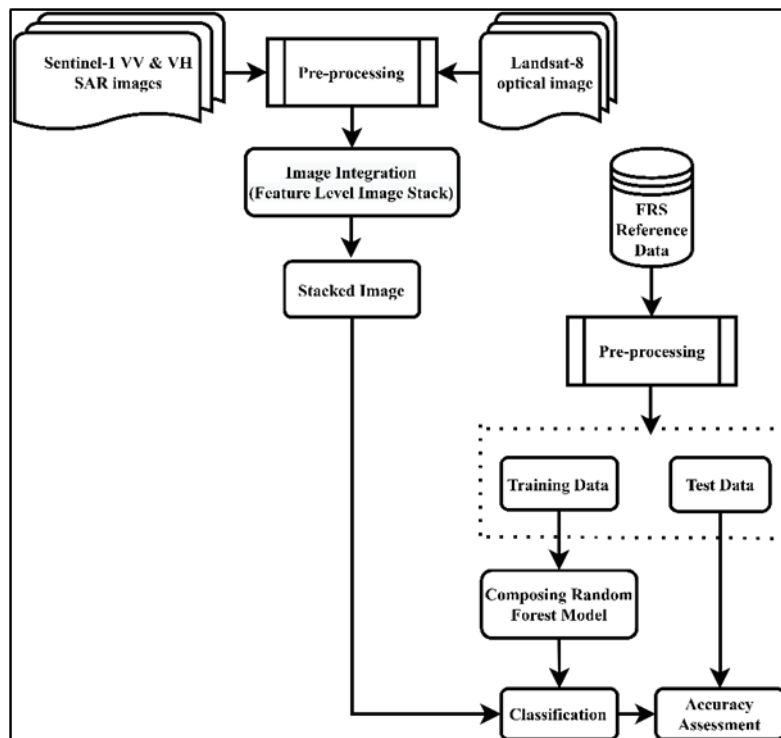


Figure 2. The flowchart of the methodology

3.1. Data pre-processing

Preprocessing operations were applied to Sentinel-1 VV and VH polarized data using the Sentinel Application Platform (SNAP) software [23]. Apply orbit file, radiometric calibration, speckle filtering (Lee Filter 5x5), topographic correction and back reflection db conversion preprocessing steps were performed. With the preprocessing applied to orbit file, the correct satellite position and velocity information was obtained by bringing up-to-date corrections to the satellite orbital state vectors of the SAR data. With radiometric calibration, the pixel values were converted to radiometrically calibrated SAR back reflection values. The speckle noise was reduced by applying a 5x5 Lee filter [24-25]. Distortions caused by topography were corrected with terrain correction and therefore the image was geometrically brought closer to the real earth. In the back-reflection dB conversion step, the back-reflection coefficients without any unit value were converted into dB using the logarithmic transformation given in Equation 1 [25].

$$\beta_{db}^0 = 10 * \log_{10}(\beta^0) \quad (1)$$

Preprocessing for the Landsat-8 optical satellite image consists of producing a layer stack of the bands to be used in classification [26]. The VV, VH and VV+VH polarized Sentinel-1 SAR data and Landsat-8 optical image obtained after the preprocessing steps are illustrated in Figure 3.

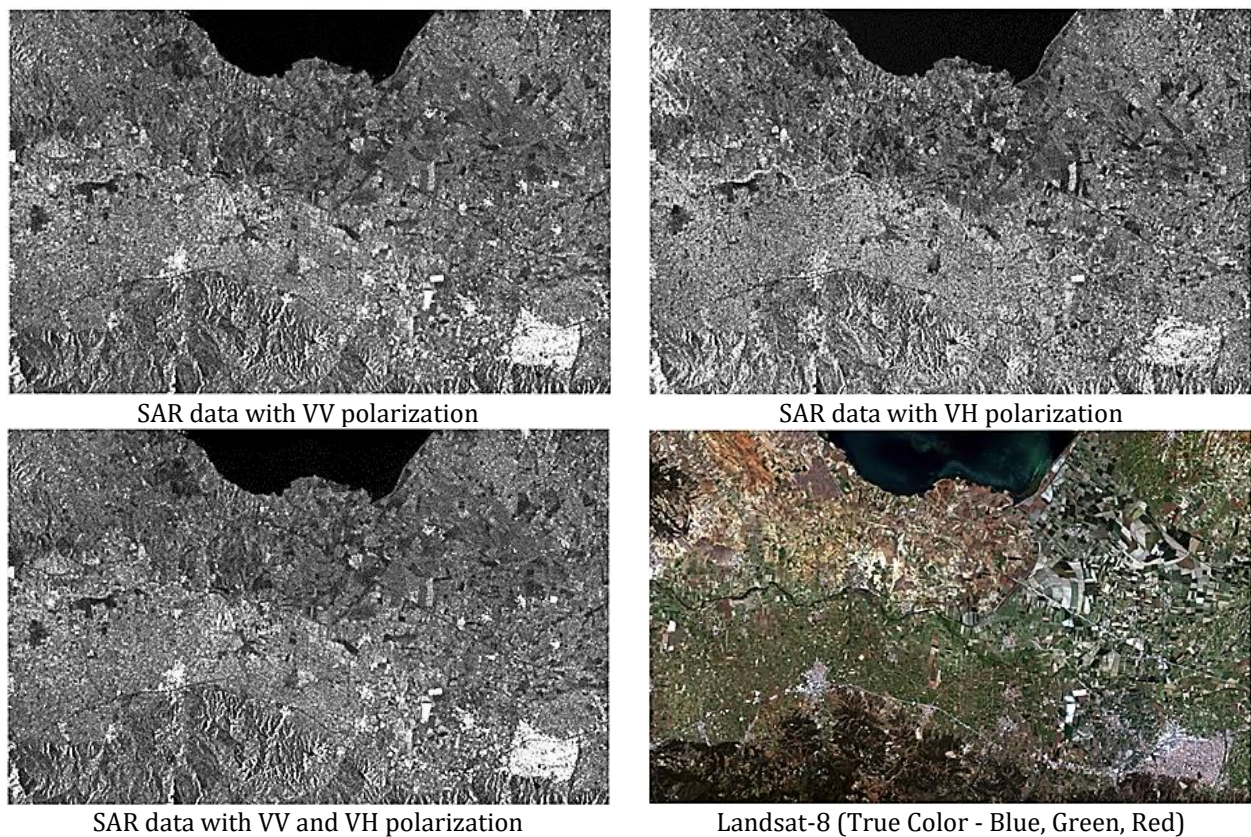


Figure 3. Landsat-8 and Sentinel-1 SAR images after pre-processing

In addition to images, the necessary preprocessing operations were also performed on the reference data (FRS data). Parcels smaller than 1000 m² were eliminated as most of these parcels did not contain a crop. The crops grown in the parcels and the spatial data of the parcels (polygon) were associated.

3.2. Integration of Sentinel-1 SAR and Landsat-8 optic images

In this study, we used feature level image integration to combine Sentinel-1 SAR (VV and VH bands) and Landsat-8 image (multi-spectral bands) data sets [27]. Our purpose for image integration was to obtain an integrated multi-band dataset from the combination of Sentinel-1 SAR image and Landsat 8 optical image. The higher spatial resolution Sentinel-1 SAR VV and VH bands were chosen as the first input data, while the lower spatial resolution multi-band (7-band) optical Landsat 8 image was chosen as the second input data. Image integration was performed using the “Composite Bands” tool of the ArcGIS software. With this tool, one can also create a raster dataset containing a subset of the original bands. This is useful if you need to create a new raster

dataset with a specific band combination and order [26]. The output raster dataset (in this study feature level integrated image) takes the cell size (spatial resolution) from the first raster band (in this study 10 m resolution Sentinel-1 SAR-VV and VH bands) in the order of inputs. Therefore, in this case, the spatial resolution of the feature level integrated data set has become 10 m.

3.3. Image classification

Image classification was carried out in MATLAB R2019b using the RF machine learning algorithm [29]. RF is one of the ensemble algorithms that uses the decision tree as the base class [30]. Before starting the tree development process, two parameters must be defined by the user to start the RF algorithm. These parameters are the number of variables (mtry) used at each node and the number of trees to be developed (ntree). The RF algorithm combines classifications made by many individual decision trees [28]. When the defined number of trees (ntree) is produced, the class of the candidate pixel is determined based on the estimation results obtained from the ntree tree [30]. In this study, the ntree value was taken as 100, and the mtry value was calculated as $\sqrt{\text{number of bands}}$ following [31]. In the present case, we used a parcel-based classification approach. In parcel-based classification, pixel groups are created according to certain characteristics of the pixels such as shape, color, texture, size, relationship and pattern, and operations are performed on these pixel groups [32-33]. In this study, we used the FRS parcel boundaries to define homogeneous pixel groups. For each parcel, the frequencies of the classified pixels were calculated and the label of the highest frequency class was assigned to all pixels falling within the parcel. Of the 1024 reference parcels, 512 were used as training and 512 were used to test the classification accuracy.

Wheat, Tomato, Corn, Corn_2, Cotton, Grapes, Clover and Olive Trees were defined as the crop types (classes) to be classified. As a result of the analysis of the images and FRS data we noticed that there were two types of corn. Therefore, corn was divided into two different classes (Corn and Corn_2). The number of parcels and pixels used for training and validation are given in Table 2. Image classification was performed using five different image data sets and the results were compared. In particular, the effect of the stacked dataset of Sentinel-1 SAR and Landsat-8 on classification accuracy was evaluated. The image data sets used for classification are as follows: i) Sentinel-1 VV band only, ii) Sentinel-1 VH band only, iii) Sentinel-1 VV and VH bands together, iv) Landsat-8 data only, and v) Stacked dataset of Sentinel-1 VV+VH bands and Landsat-8 data.

Table 2. The number of parcels and pixels used for training and validation

Agricultural Crop	Training Data (Parcel / Pixel)		Test Data (Parcel / Pixel)	
Wheat	94	37852	94	11473
Tomato	26	12880	26	4399
Corn	78	26636	78	10480
Corn_2	25	7661	25	3628
Cotton	28	15090	28	7020
Grapes	202	33996	202	14398
Clover	8	6027	8	563
Olive Trees	51	27482	51	11670
Total	512	167624	512	63631
Overall total	1024/231255			

4. Results and Discussion

For the accuracy assessment of the classified images, we used a standard error matrix. Since the classification was conducted based on parcel basis, we performed accuracy assessment on parcel-basis, therefore. In determining the number of test parcels, the study of [30] was taken into account. From the error matrix [34], we computed the overall accuracy and Kappa coefficient values. In addition, producer’s accuracy (PA) value and user’s accuracy (UA) value were also calculated for each class. The calculated accuracy values are given in Table 3. Figure 4 shows the graphical comparison of overall accuracy and Kappa coefficient values of the classified outputs. The classified images using different data sets are shown in Figure 5 (a-e).

Table 3. Classification accuracy values computed based on different data sets. (PA: Producer Accuracy, UA: User Accuracy, VV: Vertical-Vertical Polarization, VH: Vertical-Horizontal Polarization)

Crop Type	Sentinel-1 VV		Sentinel-1 VH		Sentinel-1 VV+VH		Landsat-8		Stacked Sentinel-1 VV+ VH and Landsat-8	
	PA (%)	UA (%)	PA (%)	UA (%)	PA (%)	UA (%)	PA (%)	UA (%)	PA (%)	UA (%)
Wheat	48,00	48,42	50,62	51,06	58,62	59,13	60,10	64,55	62,98	68,86
Tomato	30,57	32,11	32,23	33,86	37,33	39,21	76,16	78,33	73,06	82,08
Corn	36,76	42,59	38,76	44,91	44,89	52,01	66,28	72,73	78,13	75,54
Corn_2	22,71	25,64	23,94	27,03	27,73	31,31	81,16	80,58	89,79	88,58
Cotton	36,04	41,87	38,00	44,15	44,01	51,13	80,72	77,14	81,91	80,34
Grapes	42,99	47,41	45,33	49,99	52,50	57,90	74,19	74,87	89,27	88,31
Clover	41,51	39,79	43,78	41,96	50,70	48,60	76,12	77,76	88,60	87,10
Olive Trees	25,52	29,65	26,91	31,27	31,17	36,21	71,63	73,90	86,65	91,46
Overall Accuracy	34,12		35,98		41,67		71,18		81,46	
Kappa Coefficient	30,22		31,87		36,92		63,06		76,24	

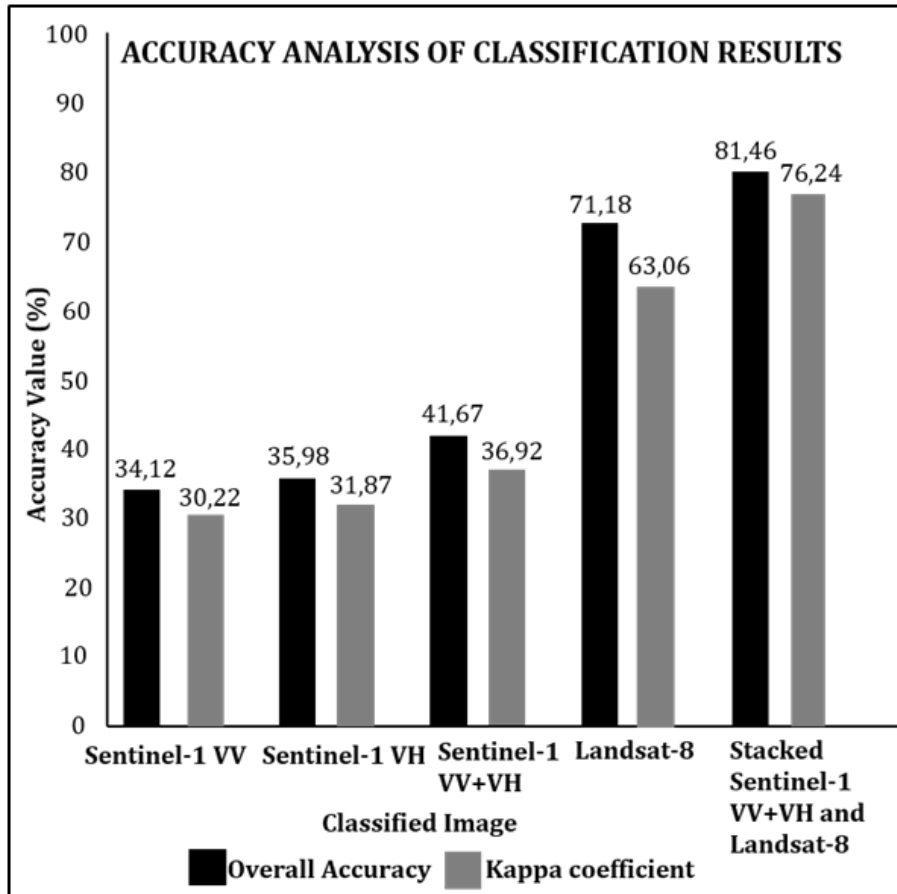


Figure 4. Overall accuracy and kappa coefficient values computed based on different data sets

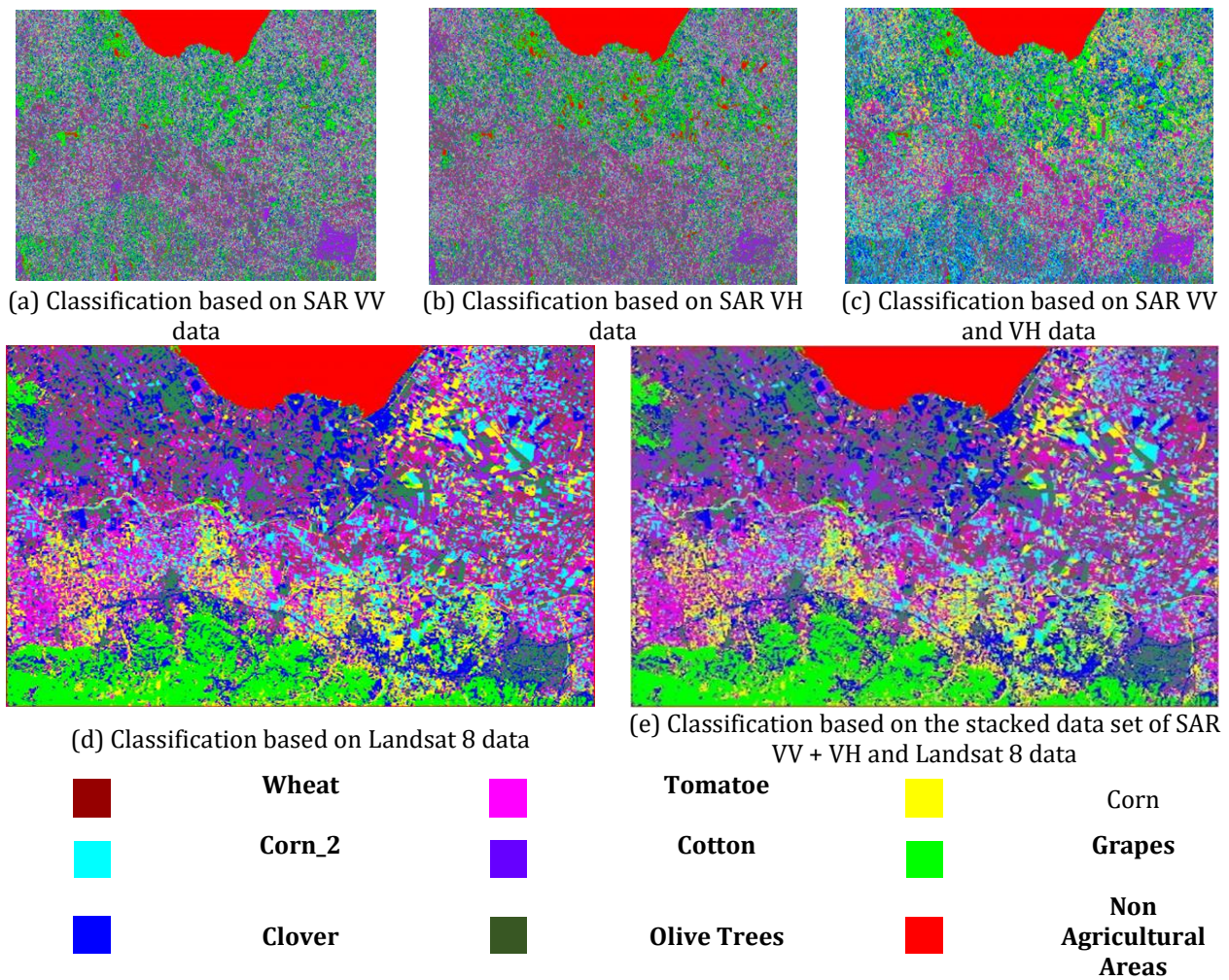


Figure 5. Comparison of the classifications conducted based on different data sets

The overall accuracy of the classification based on Sentinel-1 VV data was calculated as 34.12% and the Kappa coefficient value was calculated as 30.22%. For wheat, the PA and UA values were calculated as 48.00% and 48.42%, respectively. Similarly, these values respectively were 30.57% and 32.11% for tomato, 36.76% and 42.59% for corn, 22.71% and 25.64% for corn_2, 36.04% and 41.87% for cotton, 42.99% and 47.41% for grapes, 41.51% and 39.79% for clover, and 25.52% and 29.65% for olive trees. Corn_2 exhibited the lowest PA and UA values, while wheat provided the highest accuracy values.

The overall accuracy of the classification based on Sentinel-1 VH data was calculated as 35.98% and the Kappa coefficient value was computed as 31.87%. The PA and UA values for wheat were 50.62% and 51.06%, respectively. Similarly, these values respectively were 32.23% and 33.86% for tomatoes; 38.76% and 44.91% for corn; 23.94% and 27.03% for corn_2; 38.00% and 44.15% for cotton; 45.33% and 49.99% for grapes; 43.78% and 41.96% for clover; and 26.91% and 31.27% for olive trees. In the classification based on this data set, corn_2 exhibited the lowest PA and UA values, while wheat provided the highest accuracy values.

For the classification based on Sentinel-1 VV and VH bands separately, the values of PA, UA, overall accuracy, and Kappa coefficients generally stayed below 50%. This is due to the fact that the VV or VH band is a single-band panchromatic data that significantly affects the classification accuracy. It is evident that if only one of the Sentinel-1 VV or VH bands is used in the classification, the crops grown in this region cannot be reliably detected.

Comparing the overall accuracy values computed based on the Sentinel-1 VV and VH bands, the VH band provided approximately 1.86% better performance than the VV band. Similarly, the Kappa coefficient value computed for the VH band was slightly higher than the value computed for the VV band.

For the classification based on both Sentinel-1 VV and VH bands, the overall accuracy and Kappa coefficient values were calculated as 41.67% and 36.92%, respectively. For each crop type, the computed producer's and user's accuracy values were respectively as follows: 58.62% and 59.13% for wheat; 37.33% and 39.11% for tomato; 44.89% and 52.01% for corn; 27.73% and 31.31% for corn_2; 44.01% and 51.13% for cotton; 52.50% and 57.90% for grapes; 50.70% and 48.60% for clover; 31.17% and 36.21% for olive trees.

Classification based on the Sentinel-1 VV and VH bands together produced approximately 5% better results than using each of these bands alone. These findings confirm the generalization in this study that when there is an

increase in the number of bands included in the classification, there is a proportional increase in the classification results.

Classification based on Landsat-8 data only provided 71.18% overall accuracy and 63.06% Kappa coefficient value. The PA (60.10%) and UA (64.55%) values computed for wheat were lower than expected. For other crop types, the computed PA and UA values are respectively as follows: 76.16% and 78.33% for tomatoes; 66.28% and 72.73% for corn; 81.16% and 80.58% for corn₂; 80.72% and 77.14% for cotton; 74.19% and 74.87% for grapes; 76.12% and 77.76% for clover, and 71.63% and 73.90% for olive trees. Compared to Sentinel-1 SAR data (VV, VH and VV+VH), the Landsat-8 data provided up to 37% better performance in the overall accuracy. For Kappa coefficient, the accuracy increase was about 33% in favor of the Landsat-8 data. For the individual crop types, the UA and PA values were approximately 30% higher than that of Sentinel-1 SAR data. Although the spatial resolution of the Landsat-8 optical bands is 30 m and the spatial resolution of the Sentinel-1 VV and/or VH bands is 10 m, the classification accuracy based on Landsat-8 data was significantly higher than that of Sentinel-1 data. In this respect, we can say that the lower spatial resolution multi-band Landsat-8 optical data may be preferred to Sentinel-1 SAR data. In addition, our findings showed that the color effect of pixels or objects (agricultural parcels for this study) appears to be more important than the size (spatial resolution) factor that the pixels occupy on the ground.

Classification based on the stacked data set of Sentinel-1 VV + VH and Landsat-8 provided the overall accuracy and Kappa values of 81.46% and 76.24%, respectively. Based on the study of [37] we can say that these values are sufficient. This data set provided the highest overall accuracy and Kappa coefficient values of the datasets used. For the individual crop types, the computed PA and UA values were, respectively as follows: 62.98% and 68.86% for wheat; 73.06% and 82.08% for tomatoes; 78.13% and 75.54% for corn; 89.79% and 88.58% for corn₂; 81.91% and 80.34% for cotton; 89.27% and 88.31% for grapes; 88.60% and 87.10% for clover and 86.65% and 91.46% for olive trees. It is evident that the use of the stacked data set of Sentinel-1 VV+ VH and Landsat 8 in the classification significantly improved the results when compared the use of either of these images. The use of the stacked Sentinel-1 VV+VH and Landsat 8 data set in the classification provided much better performance than that of using either of these images (Table 3 and Figure 4).

For the classification based on Sentinel-1 VV, VH, and VV+VH, wheat provided the highest PA and UA accuracy values (Table 3). On the other hand, for the classification based on Landsat-8 and the stacked data set of Sentinel-1 VV+VH and Landsat-8, wheat gave the lowest PA and UA accuracy values. This is due to the presence of interpretation elements of SAR and optical images that may be inferior or superior to each other. The characteristics of SAR images are different from optical ones. Optical image classification is highly correlated with texture and shape information, while SAR image classification relies more on shape information because the texture is always blurred and full of noise [35]. In this study, the existence of this situation has been monitored only for the wheat crop type.

5. Conclusion and Recommendation

This study investigated the effect of the integration of single date (07.06.2017) Sentinel-1 SAR and Landsat-8 data on the classification performance of agricultural summer crops. The integration of these two data sets was carried out at feature level through image stacking and supervised RF machine learning algorithm was used for classification. Image classification was performed using different image data sets. Classification conducted using the original Sentinel-1 VV or VH polarized bands provided accuracy values about 35%. The use of both Sentinel-1 VV and VH bands in classification exhibited a marginal effect in the results increasing overall accuracy to 41.67%. The results show that a single-date Sentinel-1 SAR VV or VH data is not sufficient in detecting summer crops, at least in the area used in this study. Classification based on Landsat-8 data only provided much higher overall accuracy (71.18%) than that of Sentinel-1 data. According to [36], this accuracy value is reasonable. This higher accuracy value demonstrates that multispectral-bands have considerable contribution to classification of a single-date image.

Classification based on the stack dataset of the integrated Sentinel-1 VV + VH and Landsat-8 provided overall accuracy and Kappa values of 81.46% and 76.24%, respectively. Among the input image datasets used in this study, this data set provided the best results. When used alone, the Sentinel-1 SAR data (VV or VH band) provided considerably low accuracy values. However, when combined with Landsat 8 optical image, Sentinel-1 SAR data demonstrated a significant contribution to results.

The FRS data are prepared based on the verbal statements of the farmers. In order to use FRS data as reference data for training and accuracy assessment, it should undergo some editing operations. Those FRS parcels with missing or incorrect information such as cultivated area, cultivated crop name, difference between total parcel area and cultivated area, etc. can be automatically detected and corrected in the database.

The use of both Sentinel-1 SAR and Landsat-8 optical images in classification provides the combined effects of higher spatial resolution SAR bands and lower spatial resolution multispectral bands. Classification based on the stack dataset of the integrated image of these two data sets appears to provide sufficient accuracy values for agricultural crop type detection in regions with reasonably large agricultural fields. The study has shown that the

stacked dataset of Sentinel-1 VV+VH and Landsat-8 belonging to a single date has great potential in extracting summer crop types.

Acknowledgement

The authors would like to thank Turkish Republic of Ministry and Forestry for providing the FRS reference data.

Funding

This research received no external funding.

Author contributions

Muslum Altun: Conceptualization, Methodology, Software, Data curation, Writing-Original draft preparation, Validation. **Mustafa Türker:** Conceptualization, Visualization, Investigation, Writing-Reviewing and Editing.

Conflicts of interest

The authors declare no conflicts of interest.

References

1. Gumma, M. K., Nelson, A., Thenkabail, P. S., & Singh, A. N. (2011). Mapping rice areas of South Asia using MODIS multitemporal data. *Journal of Applied Remote Sensing*, 5(1), 1-26.
2. Thenkabail, P. S., Hanjra, M. A., Dheeravath, V., & Gumma, M. (2011). Global croplands and their water use remote sensing and non-remote sensing perspectives. Weng Q (Ed.), *Advances in Environmental Remote Sensing: Sensors, Algorithms, and Applications*, (pp. 383-419). Florida, CRC Press.
3. Viskovic, L., Kosovic, I. N., & Mastelic, T. (2019, September). Crop classification using multi-spectral and multitemporal satellite imagery with machine learning. In *2019 International Conference on Software, Telecommunications and Computer Networks (SoftCOM)* (pp. 1-5). IEEE.
4. Altun, M. & Türker, M. (2021). Çoklu zamanlı Sentinel-2 görüntülerinden tarımsal ürün tespiti: Mardin – Kızıltepe örneği. *Afyon Kocatepe Üniversitesi Fen Ve Mühendislik Bilimleri Dergisi*, 21 (4), 881-899.
5. Lemoine, G., & Leo, O. (2015, November). Crop mapping applications at scale: Using google earth engine to enable global crop area and status monitoring using free and open data sources. In *International Geoscience and Remote Sensing Symposium, (IGARSS)* (pp. 1496-1499). IEEE.
6. Lussem, U., Hütt, C., & Waldhoff, G. (2016, July). Combined analysis of Sentinel-1 and Rapid Eye data for improved crop type classification: An early season approach for rapeseed and cereals. *International Archives of the Photogrammetry, Remote Sensing and Spatial Information Sciences*, 41(2016), 959-963.
7. Foody, G. M., M. B. McCulloch, M. B., & W. B. Yates, W.B. (1994). Crop classification from C-band polarimetric radar data. *International Journal of Remote Sensing*, 15(14), 2871-2885.
8. Skriver, H. (2012). Crop classification by multitemporal C- and L-band single- and dual polarization and fully polarimetric SAR. *IEEE Transactions on Geoscience and Remote Sensing*, 50(6), 2138-2149.
9. Sonobe, R., Tani, H., Wang, X., Kobayashi, N., & Shimamura, H. (2014). Random forest classification of crop type using multi-temporal TerraSAR-X dual-polarimetric data. *Remote Sensing Letters*, 5(2), 157-164.
10. Siachalou, S., Mallinis, G., & Tsakiri-Strati, M. (2015). A hidden markov models approach for crop classification: Linking crop phenology to time series of multisensor remote sensing data. *Remote Sensing*, 7(4), 3633-3650.
11. Altun, M. & Türker, M. (2022). Kaynaştırılmış Sentinel-1 SAR ve Landsat-8 optik veriden makine öğrenme algoritması ile tarımsal ürün tespiti . *Turkish Journal of Remote Sensing and GIS*, 3 (1) , 1-19.
12. Chen, S., Useya, J., & Hillary Mugiyi, H. (2020). Decision-level fusion of Sentinel-1 SAR and Landsat 8 OLI texture features for crop discrimination and classification: case of Masvingo, Zimbabwe. *Heliyon*, 6(11), 1-14.
13. Nuthammachot, N., & Stratoulas, D. (2019). Fusion of Sentinel-1A and Landsat-8 images for improving land use/land cover classification in Songkla Province, Thailand. *Applied Ecology and Environmental Research*, 17(2), 3123-3135.
14. Otukei, J. R., Blaschke, T., & Collins, M. (2015). Fusion of TerraSAR-x and Landsat ETM+ data for protected area mapping in Uganda. *International Journal of Applied Earth Observation and Geoinformation*, 38, 99-104.
15. Suwarsono, N., Prasasti, I., Nugroho, J. T., Sitorus, J., & Triyono, D. (2018). Detecting the lava flow deposits from 2018 anak Krakatau eruption using data fusion Landsat-8 optic and Sentinel-1 SAR. *International Journal of Remote Sensing and Earth Sciences*, 15(2), 157-166.

16. Dimov, D., Kuhn, J., & Conrad, C. (2016, July). Assessment of cropping system diversity in the fergana valley through image fusion of Landsat 8 and Sentinel-1. In 23rd ISPRS Congress, 2016. (pp.173-180). XXIII ISPRS.
17. Cao, J., Cai, X., Tan, J., Cui, Y., Xie, H., Liu, F., Yang, L., & Luo, Y. (2020). Mapping paddy rice using Landsat time series data in the Ganfu Plain irrigation system, Southern China, from 1988-2017. *International Journal of Remote Sensing*, 42(4), 1556-1576.
18. Forget, Y., Shimoni, M., Gilbert, M., & Linard, C. (2018). Complementarity Between Sentinel-1 and Landsat 8 Imagery for Built-Up Mapping in Sub-Saharan Africa. 10.20944/preprints201810.0695.v1.
19. Zhang, H., & Xu, R. (2018). Exploring the optimal integration levels between SAR and optical data for better urban land cover mapping in the Pearl River Delta. *International Journal of Applied Earth Observation and Geoinformation*, 64(2018), 87-95.
20. Copernicus. (2021, Mart 30). Copernicus Open Access Hub. <https://scihub.copernicus.eu/dhus/#/home>
21. EarthExplorer. (2021, Mart 30). USGS Earth Explorer. <https://earthexplorer.usgs.gov>
22. T.C. Tarım ve Orman Bakanlığı. (2021, Mart 30). T.C. Tarım ve Orman Bakanlığı. <https://www.tarimorman.gov.tr/>
23. ESA Copernicus Open Access Hub. (2021, Mart 30). Overview, Sentinel-1 Data Offer. <https://scihub.copernicus.eu/userguide/>
24. Lee, J.S., Jurkevich, I., Dewaele, P., Wambacq, P., & Oosterlinck, A. (1994). Speckle filtering of synthetic aperture radar images: A review. *Remote Sensing Reviews*, 8(4), 313-340.
25. Filipponi, F. (2019). Sentinel-1 GRD preprocessing workflow. *Multidisciplinary Digital Publishing Institute Proceedings*, 18(1), 11-15.
26. ArcGIS User Guide. (2021, Nisan 22). ArcGIS Desktop User Guide Documentation, <https://desktop.arcgis.com/en/documentation/>
27. Erdas Imagine User Guide. (2021, Nisan 22). Hexagon Erdas imagine user guide. <https://www.hexagongeospatial.com/>
28. Witharana, C., Civco, D. L., & Meyer, T. H. (2013). Evaluation of pansharpening algorithms in support of earth observation based rapid-mapping workflows. *Applied Geography*, 37(2013), 63-87.
29. MathWorks. (2021, Mayıs 8). MathWorks Makers of MATLAB and Simulink. <https://www.mathworks.com/>
30. Liaw, A., & Wiener, M. (2002). Classification and regression by random forest. *R News*, 2(3), 18-22.
31. Pal, M. (2005). Random forest classifier for remote sensing classification. *International Journal of Remote Sensing*, 26(1), 217-222.
32. Utgoff, P. E., & Brodley, C. E. (1990). An incremental method for finding multivariate splits for decision trees. In *Machine Learning Proceedings 1990*, (pp. 58-65), Morgan Kaufmann.
33. Pal, M., & Mather, P. M. (2003). An assessment of the effectiveness of decision tree methods for land cover classification. *Remote Sensing of Environment*, 86(4), 554-565.
34. Campbell, J.B., & Wynne, R.H. (1996). *Introduction to remote sensing*. New York, London, Guilford Press.
35. Guo, Y., Pan, Z., Wang, M., Wang, J., & Yang, W. (2020). Learning Capsules for SAR Target Recognition. *IEEE Journal of Selected Topics in Applied Earth Observations and Remote Sensing*, 13(1), 4663-4673.
36. Cohen, J. (1960). A coefficient of agreement for nominal scales. *Educational and Psychological Measurement*, 20(1), 37-46.



© Author(s) 2022. This work is distributed under <https://creativecommons.org/licenses/by-sa/4.0/>





Advanced Remote Sensing

<http://publish.mersin.edu.tr/index.php/arcej>

e-ISSN 2979-9104



Analyzing rice farming between sowing and harvest time with Sentinel-1 SAR data

Ahmet Batuhan Polat ^{*1}, Fusun Balik Sanli ², Ozgun Akcay ¹

¹Canakkale Onsekiz Mart University, Department of Geomatics Engineering, Türkiye, abpolat@comu.edu.tr, akcay@comu.edu.tr

²Yildiz Technical University, Department of Geomatics Engineering, Türkiye, fbalik@yildiz.edu.tr

Cite this study: Polat, A. B., Şanlı, F. B., & Akçay, O. (2022). Analyzing rice farming between sowing and harvest time with Sentinel-1 SAR data. *Advanced Remote Sensing*, 2 (1), 34-39

Keywords

Remote sensing
Synthetic-aperture radar
Rice
Time-series analysis
Backscatter

Research Article

Received: 25.05.2022

Revised: 22.06.2022

Accepted: 27.06.2022

Published: 30.06.2022

Abstract

Agriculture has always been in an important position throughout human history. Today, the development of technology has accelerated studies to increase productivity in agriculture. With the use of remote sensing in agriculture, different crop types in large regions could be observed and their differences from each other could be examined with a spectral sight. With the observations obtained, instant surface monitoring in the agricultural sector makes it possible to perform analyzes. In the study, the paddy fields, where the rice product was named at the time of first planting, were examined by remote sensing method. Differences in Synthetic Aperture Radar (SAR) observations were analyzed between the first crop sowing and harvest time. In addition, in order to check the consistency of the results, the differences in the values obtained according to the representation of the samples distributed in the field were determined. Considering the results, it was seen that the lowest backscatter values were obtained for the paddy fields in the 35-day period after the first planting time and these values increased as the harvest time approached. There is an approximately 69% change in the lowest and highest mean backscatter values. Finally, when the time series analysis is performed according to the control samples in the field, it has been determined that the points represented by a single pixel have a more irregular distribution comparing the samples obtained in the form of polygons. This shows that pixels cannot be evaluated independently due to noise in SAR data.

1. Introduction

Rice is a food source for more than half of the world's population [1]. Paddy fields planted to obtain rice mature in about 130 days and become ready for harvest [2]. Agricultural applications such as plant health monitoring, estimating water stress, and sensitive classification of different agricultural products are carried out with remote sensing satellites [3-5]. Radar satellites have started to be used in this field as much as optical satellites, especially due to their advanced features [6]. One of the biggest advantages of radar images is that they do not contain some of the restrictions found in optical images. It is not possible to use optical images, especially in bad weather conditions. However, radar images work even in cloudy weather conditions [7].

Radar images can be used in different applications for the detection of water surfaces since they record differences in backscatter values according to surface properties [8]. Especially for crop yield, backscatter (dB) values obtained in Synthetic Aperture Radar (SAR) system are used [9]. In the paddy fields, water is used intensively from the first planting time to the harvest time [10]. There are different studies using SAR backscatter values in paddy fields [11-13]. The water level is monitored with the radar backscatter values and the process of the rice production in the paddy field can be followed from the moment of sowing to the harvest time. In the study

of Kim et al. [13] the backscatter values obtained with different radar bands such as X, C and L and different incidence angles in rice fields were investigated. As a result of the observations, they emphasized that different backscatter values can be found with different incidence angles and emphasized that the values obtained with different polarization types may vary according to the period between sowing and harvesting of the product [14]. In the study conducted by Phan et al. [12], one of the agricultural regions of Vietnam were examined. As a result of a 5-year time series analysis in the study, they concluded that the backscatter values constantly progressed in the same profile. They also stated that they could not obtain consistent results when the crop sowing and harvesting times were different in the same region [12].

The aim of this study is to examine the rice cultivation in the Thrace region between May and October with multi-time images obtained from the Sentinel-1 SAR satellite. For that purpose, evaluating and analyzing the backscatter values obtained during the period between planting and harvesting according to months is the main object of the study.

2. Material and Method

Within the scope of the study, firstly the study area was determined; then Sentinel-1 SAR data, which passes through the same region every 12 days, was obtained for the study area. After that, preprocessing steps were carried out in order to remove the noise and for the improvement of the image. Then, the obtained images were combined and the average backscatter values were examined and the period between sowing and harvesting time was examined in the form of a time series table.

2.1. Study Area and Dataset

The İpsala district of Edirne province was chosen as the study area. Edirne province has more than 40% of the cultivated paddy fields in Turkey, while the district of İpsala has more than 17% of the cultivated paddy fields in Turkey [12]. The data used is the Sentinel-1 SAR satellite data, available free of charge from the European Space Agency (ESA). 15 SAR images taken every 12 days at equal intervals from the paddy planting time of May to the end of the paddy harvest time of October were used. The study area is shown in Figure 1. In Figure 2, SAR images are shown which are used for the study.

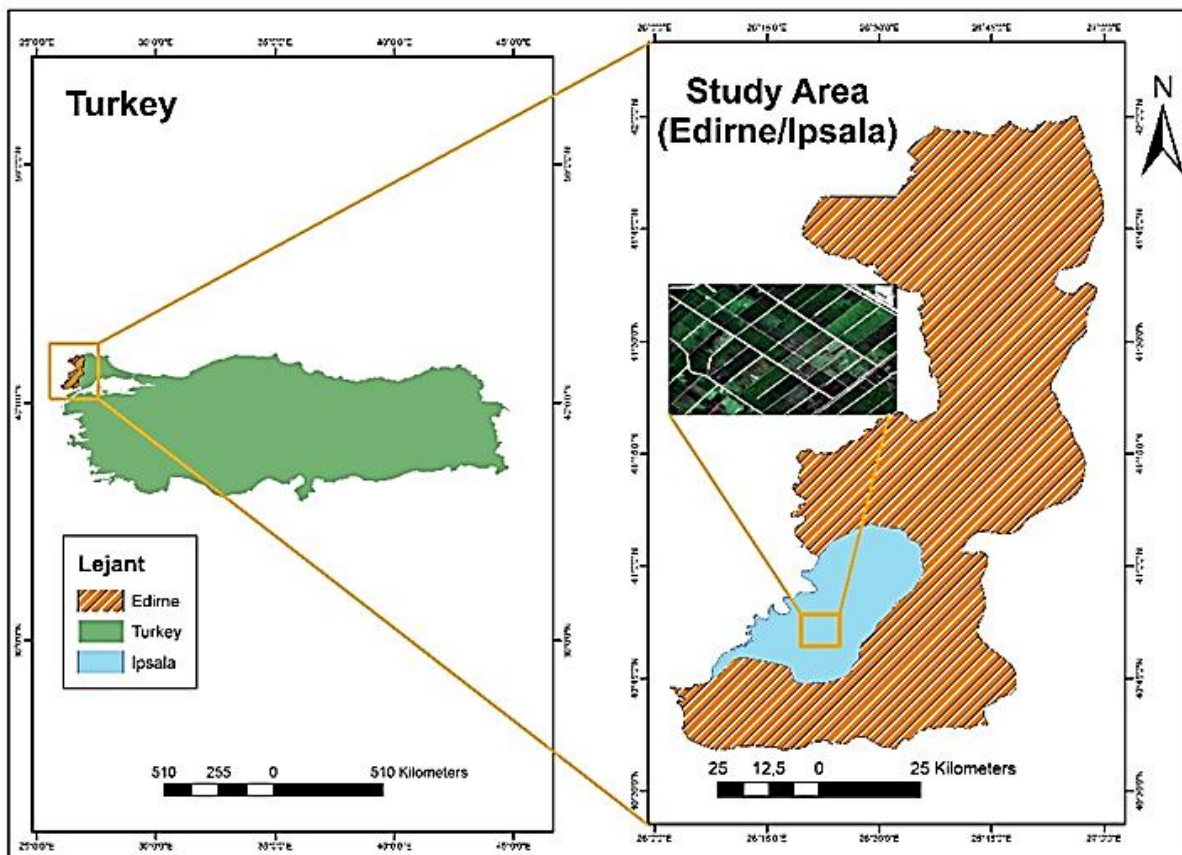


Figure 1. Study Area

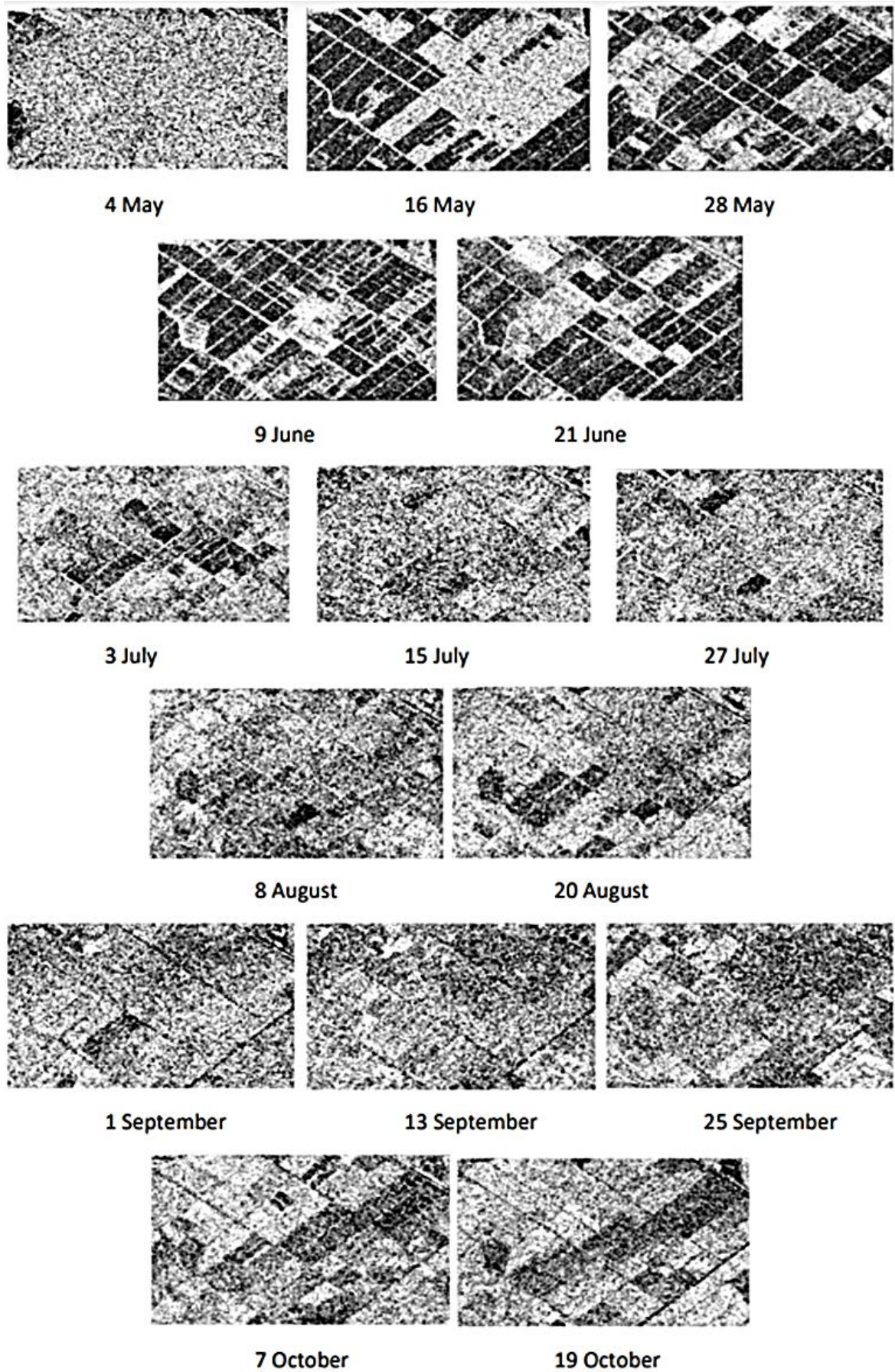


Figure 2. SAR Dataset

2.2. Data Preprocess

SAR images are not suitable for direct use as they are raw data. For this reason, they must first go through a number of pre-processing steps. First, thermal noises in the image are eliminated. Then, orbit files were applied for georeferencing. Afterwards, the calibration process was performed in order to obtain the backscatter values from the image. Finally, terrain correction was performed for the coordinate correction process and the images were ready. The preprocessing steps are shown in Figure 3.

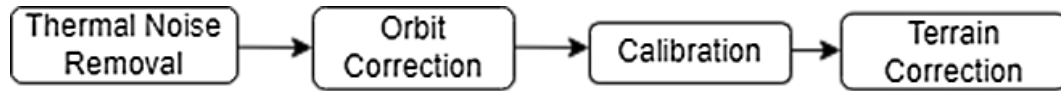


Figure 3. Preprocessing steps

After the preprocessing steps, the backscatter (dB) values in the images were recorded separately for all dates. After that, Sentinel-1 SAR data were combined to analyze all the data together. A reference master data is needed for the stacked data. For this reason, the data dated May 4 which is the sowing time was determined as the master image, and all remaining data were selected as slave images. Then, a time-series graph covering all dates was obtained and control samples were placed in certain areas of the field as single-pixel and polygon areas, respectively. The results were compared over these samples and the process of the paddy fields were examined. Control samples obtained as points and areas in the study area are given in Figure 4.

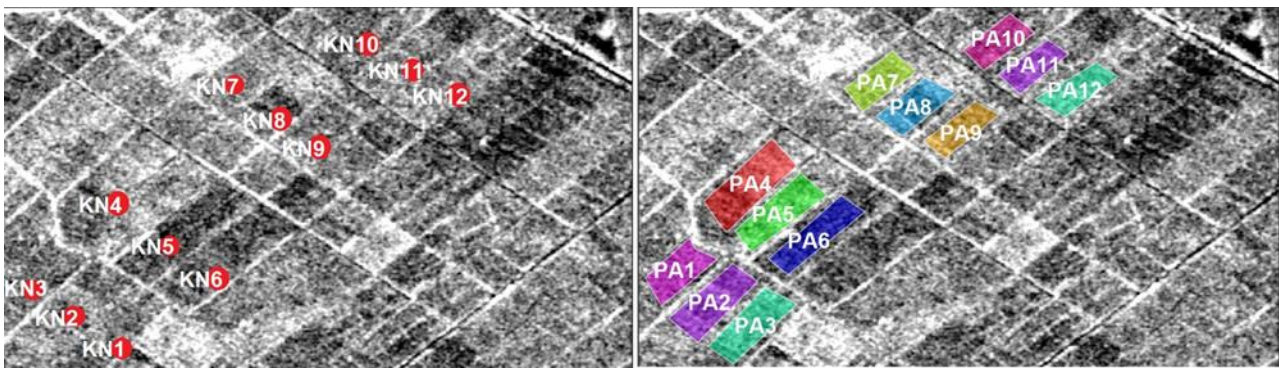


Figure 4. Control samples were taken in the field (Respectively, in the left image, the dots represent a single pixel, and in the right image, they represent approximately one crop parcel)

3. Results

Backscattering (dB) values obtained from the dataset are given in Table 1.

Table 1. Backscatter (dB) values obtained from the dataset

Image Acquisition Date (2021)	Maximum Backscatter(dB) Value	Minimum Backscatter(dB) Value	Average Backscatter(dB) Value
4 May	-9.6361	-30.6967	-20.0439
16 May	-7.0947	-34.8829	-23.4318
28 May	5.8827	-33.2257	-23.0120
9 June	-10.0764	-35.4931	-23.6802
21 June	-11.2858	-34.4223	-22.6449
3 July	-10.4948	-32.1491	-20.5596
15 July	-9.6795	-28.4936	-18.7282
27 July	-10.0417	-32.2956	-19.9034
8 August	-6.5182	-30.7698	-19.3219
20 August	-10.3978	-29.2372	-18.7064
1 September	-8.4526	-28.6447	-17.5985
13 September	-8.3038	-28.3478	-18.0371
25 September	-7.9786	-28.9482	-18.7683
7 October	-9.1572	-30.4993	-18.4484
19 October	-6.5108	-28.1091	-16.4259

Considering the backscatter (dB) values, the lowest average value was -23.6802 on the 9 June, while the highest average was -16.4259 after the harvest time which the date of 19 October.

4. Discussion

According to the results examined in Table 1, while the lowest level of backscattering values was obtained with field irrigations after the first planting time, the backscatter values begin to increase as the crop dries up at the harvest time and as the drying process takes place. The results we found gave similar results to the study by Phan et al. However, in this study, we have determined that analyzing SAR data with a single pixel can yield inconsistent results, so it would be more accurate to analyze within one area.

The time series tables extracted from the control samples obtained from the field are given in Figure 5.

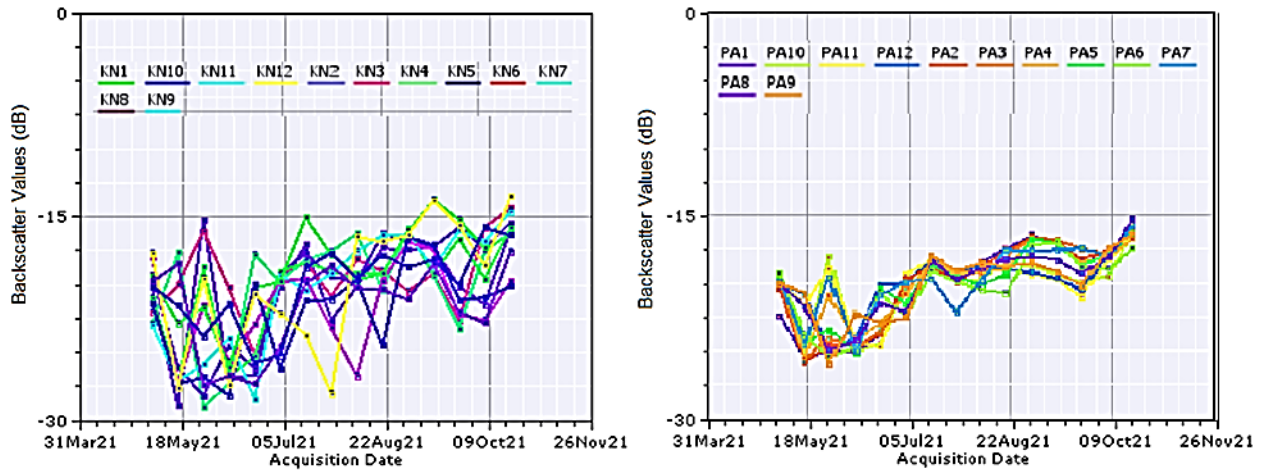


Figure 5. Time series plots obtained from control samples (Respectively, samples representing a single pixel are used in the left chart, while samples covering the area are used in the right chart)

5. Conclusion

In this study, the process of rice, which is an important source of nutrition, from the first planting to the harvest time was examined with SAR images. When the obtained results are examined, it has been observed that the backscatter values on the radar satellites can determine the stage between sowing and harvesting due to the intense demand for water during the growing process of the paddy fields. Again, when examining the backscatter values in radar images, it has been seen that choosing a polygon area instead of a single-pixel representation will give more objective results by choosing an average value. The reason for this is that the excess noise in radar images can detect very different values from each other even in pixels that are next to each other.

Funding

This research received no external funding.

Author contributions

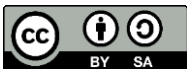
Ahmet Batuhan Polat: Methodology, Writing, Literature, Software **Fusun Balik Sanli:** Validation, Editing. **Ozgun Akcay:** Validation, Editing, Methodology.

Conflicts of interest

The authors declare no conflicts of interest.

References

1. Kuenzer, C., & Knauer, K. (2013). Remote sensing of rice crop areas. *International Journal of Remote Sensing*, 34(6), 2101-2139.
2. İpsala District Governorship (2021). Çeltik, [Access Date: 11.01.2022], <http://www.ipsala.gov.tr/pirinc>
3. Jamshidi, S., Zand-Parsa, S., & Niyogi, D. (2021). Assessing crop water stress index of citrus using in-situ measurements, Landsat, and Sentinel-2 Data. *International Journal of Remote Sensing*, 42(5), 1893-1916.
4. Shafi, U., Mumtaz, R., Iqbal, N., Zaidi, S. M. H., Zaidi, S. A. R., Hussain, I., & Mahmood, Z. (2020). A Multi-Modal Approach for Crop Health Mapping Using Low Altitude Remote Sensing, Internet of Things (IoT) and Machine Learning. *IEEE Access*, 8, 112708-112724
5. Ustuner, M., Sanli, F. B., Abdikan, Saygin, Esetlili, M. T., & Kurucu, Y. U. S. U. F. (2014). Crop type classification using vegetation indices of rapideye imagery. *The International Archives of Photogrammetry, Remote Sensing and Spatial Information Sciences*, 40(7), 195.
6. Dingle Robertson, L., Davidson, A., McNairn, H., Hosseini, M., Mitchell, S., De Abelleira, D., ... & Cosh, M. H. (2020). Synthetic Aperture Radar (SAR) image processing for operational space-based agriculture mapping. *International Journal of Remote Sensing*, 41(18), 7112-7144.
7. Tong, X., Luo, X., Liu, S., Xie, H., Chao, W., Liu, S., ... & Jiang, Y. (2018). An approach for flood monitoring by the combined use of Landsat 8 optical imagery and COSMO-SkyMed radar imagery. *ISPRS journal of photogrammetry and remote sensing*, 136, 144-153.
8. Polat, A. B., & Akcay, Ö. (2021). Rapid Flood Mapping with Sentinel-1 SAR Images: A Case Study of Maritsa River. *2nd Intercontinental Geoinformation Days (IGD)*, 123-126, Mersin, Turkey.
9. Wang, J., Dai, Q., Shang, J., Jin, X., Sun, Q., Zhou, G., & Dai, Q. (2019). Field-scale rice yield estimation using sentinel-1A synthetic aperture radar (SAR) data in coastal saline region of Jiangsu Province, China. *Remote Sensing*, 11(19), 2274.
10. Uphoff, N. (2006). The system of rice intensification (SRI) as a methodology for reducing water requirements in irrigated rice production. *International Dialogue on Rice and Water: Exploring Options for Food Security and Sustainable Environments*, 1-23.
11. Nguyen, D. B., & Wagner, W. (2017). European rice cropland mapping with Sentinel-1 data: The Mediterranean region case study. *Water*.
12. Phan, H., Le Toan, T., & Bouvet, A. (2021). Understanding Dense Time Series of Sentinel-1 Backscatter from Rice Fields: Case Study in a Province of the Mekong Delta, Vietnam. *Remote Sensing*, 13(5), 921.
13. Kim, Y. H., Hong, S. Y., & Lee, H. (2008, July). Radar backscattering measurement of a paddy rice field using multi-frequency (L, C and X) and full-polarization. In *IGARSS 2008-2008 IEEE International Geoscience and Remote Sensing Symposium (Vol. 4, pp. IV-553)*. IEEE.
14. Yazıcı, E. (2020). Durum ve Tahmin, PİRİNÇ. TEPGE, <https://arastirma.tarimorman.gov.tr/tepge/Menu/36/Durum-Ve-Tahmin-Raporlari>. [Access Date: 12.01.2022].



© Author(s) 2022. This work is distributed under <https://creativecommons.org/licenses/by-sa/4.0/>